Fallowed Heat Island: High surface temperature from fallowed agricultural lands increases nearby water demand and reduces crop yield.

Md. Minhazul Kibria[1], Adeyemi A. Adebiyi[1], John T. Abatzoglou[2]

[1]*Department of Life and Environmental Sciences, University of California, Merced* mkibria@ucmerced.edu
[2]*Department of Management of Complex Systems, University of California, Merced.* jabatzoglou@ucmerced.edu

*Corresponding author: Adeyemi A. Adebiyi
Email: aaadebiyi@ucmerced.edu

Abstract

Agricultural land fallowing is a practice of temporarily idling farmlands to maximize soil water storage, restore plant nutrients, and minimize soil erosion hazards. Despite the benefits of land fallowing, it remains unclear to what extent it affects nearby crop productivity. Here, we show that one such effect is through the *fallowed heat island*, a concept similar to urban heat island, whereby exposed fallowed agricultural lands absorb solar radiation and retain heat more than their surrounding irrigated croplands. Using high-resolution satellite-based surface temperature and evapotranspiration information over California's Central Valley, we find that the fallowed heat island effects raise the summer surface temperature of nearby agricultural fields by as much as 6°C. In addition, this effect also results in

a significant evapotranspiration deficit of up to -60 mm in the adjacent agricultural croplands, corresponding to almost 40% additional water demand compared to ideal conditions. Furthermore, we also find that the compound temperature-moisture effects of the fallowed heat island result in a reduction of up to 5% in corn crop yield relative to the county-level baseline. Overall, our findings have significant implications for sustainable water management policies and for spatially informed agricultural planning that considers changes in local microclimates.

Significance Statement

Fallowing agricultural land is widely practiced by farmers to conserve water and restore soil health, but its consequences for nearby crops remain largely unexplored. We demonstrate that fallowed fields create a localized heat island effect, which over adjacent croplands results in higher surface temperatures, drier soil moisture, increases in water demand, and reductions in crop yields compared to baseline irrigated croplands. Our findings reveal a critical trade-off in sustainable farming: water conservation through land fallowing may inadvertently impose heat and water stress on neighboring productive croplands, highlighting the need for spatially coordinated agricultural planning that maximizes crop yield.

Introduction

The concept of a *heat island* defines an area with a significantly higher surface or atmospheric temperature relative to its surrounding environment, with scales that can range from a few hundred meters to a few kilometers (1–4). At the kilometer scale, this concept of heat island has previously been applied to urban environments, where rapid infrastructural changes and exposure to built infrastructures, including pavements, buildings, and roads, have resulted in a rise in land surface temperature relative to surrounding rural or suburban areas (2, 5). Specifically, these exposed urban surfaces absorb solar radiation, and due to their lower albedo, they can retain more energy within their structure compared to vegetated green surfaces in rural areas (1). In addition, in some densely built urban areas, the movement of air becomes limited due to the closely packed structures, which leads to poor ventilation and eventually an increase in air temperature (6). While several studies have focused on urban heat islands with built surfaces, the concept of heat islands resulting from land cover changes extends beyond urban boundaries and non-concrete environments, particularly at small scales. For example, previous studies have shown that heat islands can occur around photovoltaic (PV) installations and, when placed in non-urban environments, could affect nearby natural ecosystems (7–9). Like urban heat islands, these studies suggest that a photovoltaic heat island occurs due to the increased absorption of solar radiation resulting from the decreased albedo of the solar panels compared to their surrounding environments. Beyond the influence of rural exposed areas on urban heat island effects, there are likely other local heat island effects in rural areas that can also have consequences for nearby communities and ecosystems that are yet to be explored (10).

Such localized heating in agricultural areas would be in contrast to the irrigation cooling that has previously been shown in the literature (11–13). Unlike urban areas, where built surfaces intensify heating, irrigated agricultural lands often create a cooling effect through enhanced evapotranspiration (13). This cooling effect depends on factors such as crop type,

planting density, and irrigation practices, which all indirectly influence the local microclimate (13, 14). For example, the surface shading from vegetation canopy reduces heat gain and storage in soils in agricultural cropland. Consequently, the energy absorbed by vegetation and surface soils can be released as latent heat during the transition of liquid water to water vapor in the atmosphere through evapotranspiration (15), which further cools the surface (16). In contrast, more drastic measures, such as temporary fallowing – where a portion of the cropland is kept unplanted for a specific period (17–19) either for improving soil health and recharge (19, 20) or for water conservation, can reverse this cooling effect and are hypothesized to similarly have significant impacts on microclimates. Depending on the surface cover or lack thereof, fallowed agricultural lands can store radiant energy from the sun throughout the day due to their low specific heat capacity and reduced evapotranspiration, resulting in higher surface temperatures (21, 22). We show an example of this localized heating effect in Figure 1 with the difference in the surface temperature between a fallowed area and surrounding agricultural cropland in Fresno County at the heart of California's Central Valley (Fig. 1a-c & Fig. S1a). In this case, the fallowed land surface has about 10-15 °C higher temperature than the surrounding agricultural cropland (Fig. 1c). Like urban heat islands, we refer to this significantly higher surface temperature at the fallowed location relative to its surrounding croplands as a *fallowed heat island*.

While fallow lands induce the heat islands, several factors can influence farmers' decisions to fallow their lands, including soil degradation and nutrient depletion (23), water management and availability (24), economic factors and market dynamics (25), government policies (26), and environmental factors, including water scarcity (27, 28). For example, due to groundwater overdrafts on water-intensive croplands in arid and semi-arid regions, fallowing is done to allow the soil to rest, regenerate nutrients, improve organic matter content, and disrupt pest and disease cycles (29) and to conserve available groundwater (30). In California's Central Valley, persistent groundwater depletion has become exacerbated in recent years with chronic drought events, resulting in the enactment of the Sustainable Groundwater Management Act (SGMA) in 2014 – a law that aims to bring groundwater basins to sustainability by 2040 (26, 30, 31). However, a major consequence of this law is that it resulted in proposed land fallowing in the Central Valley as one strategy to achieve groundwater balance (17).

Regardless of the reasons for land fallowing of agricultural lands, the presence of a nearby fallowed heat island, and the eventual higher temperatures they produce (Fig. 1c), may potentially affect crop water demand, crop yield, and productivity of adjacent agricultural lands (32, 33). Specifically, high temperatures increase transpiration rates (34), and where plants lack sufficient water to support growth and development, this can result in reduced crop yields (35). While different crops respond to temperature changes in different ways, excessively high temperatures almost always negatively impact crop yield by accelerating crop phenology, shortening grain-filling periods, and reducing biomass accumulation, which ultimately leads to decreased crop yields (36–38). For temperature-sensitive crops such as corn and tomatoes, even brief periods of heat stress during key growth stages can result in significant yield penalties (39). Despite the potential impacts of excessively nearby high temperatures on crop water demand and yield, the concept of the fallowed heat island

from fallow lands has previously not been explored, to our knowledge, nor has the extent of temperature change it could produce relative to nearby agricultural croplands been estimated.

To fill this gap, we focus on California's Central Valley, an extremely productive agricultural hub that grows an abundance of high-value crops and contains about 17% of all U.S. irrigated croplands (40). In California, the Central Valley accounts for 75% of irrigated croplands (Fig. S1a-c), and as a result, it also accounts for the majority (77%) of fallow lands in the state (17). These fallowed lands occupy about 45% of the total croplands in some counties (Fig. 1d and Fig. S1). As a result, the Central Valley serves as a natural testbed to understand the impacts of heat island effects of fallowed lands on nearby cropland. Consequently, using observational datasets that leverage satellite information, we obtained crop type information, including fallow lands (41), land surface temperature, surface bareness information (42, 43), and evapotranspiration (44) between 2013 and 2022 (see Methods). We find that fallowed heat islands are indeed ubiquitous in California's Central Valley, resulting in significantly warmer surface temperatures than the surrounding agricultural croplands. We also find that this increased surface temperature due to fallowed heat island results in significant increases in evapotranspiration deficit and crop water demand that consequently reduce the overall crop yield.

Results

Fallowed Heat Islands:

We define fallowed heat islands as fallowed or idled fields that are significantly warmer than their surrounding agricultural croplands. To understand the intensity of fallowed heat islands and how it may affect their surrounding croplands, we first seek to assess the baseline surface temperature of fallowed areas different from their non-fallowed agricultural croplands in California's Central Valley. To do so, we estimate the percentage of fallowed and non-fallowed croplands that are within certain surface temperature thresholds. We find that fallowed lands are more likely to have extreme temperatures of 50°C or higher than non-fallowed agricultural croplands, which typically remain below 40 °C (Fig. 1f). In addition, we also find that this percentage difference is higher in the southern part of San Joaquin Valley (R1) than the northern part of San Joaquin Valley and Metro Sacramento (R2) or the northern part of Sacramento Valley (R3). This indicates a latitudinal shift in high temperatures associated with fallowed lands (Fig. 1e & Fig. S2). Further, fallowed lands also exhibit a similar latitudinal shift in surface bareness (Fig. S3), which correlates with surface temperature (> 0.8; Fig. S4). This result suggests that the coupling between surface temperature and bareness could result in a potential feedback process, where a sparsely vegetated surface absorbs more heat, leading to the drying out of remaining vegetation and increased surface exposure, which in turn allows for more heat to be absorbed by the surface.

Although the results above show, on average, that fallowed lands across the California Central Valley are generally hotter and are exposed to heat than non-fallowed croplands, it does not explain the effects of the fallowed heat island, whereby the heat absorbed impacts

its nearby agricultural non-fallowed croplands. To address this, we obtained the surface temperature values of non-fallowed croplands centered around 900-m^2 fallowed fields across the Central Valley (Fig. 2). The result shows that the fallowed land exhibits significantly higher surface temperature than the surrounding agricultural croplands (Fig. 2a; Fig. S5). Specifically, on average, we find that the fallowed lands could have surface temperatures of up to 55 °C, which is about 4-10°C warmer than the surrounding agricultural croplands. In addition, we also find that the heat from the fallow field creates a cone-like structure and radially spreads outwards, similar to the urban heat islands, thereby validating our hypothesis of the fallowed heat island (Figs. 2a; Fig. S5).

Furthermore, we estimate the intensity (ΔT) of the fallowed heat island as the change in the surface temperature away from the fallowed center relative to a reference location over the nearby consecutively connected agricultural croplands (see Methods). We define a reference location as the location of the first minimum surface temperature, away from the fallowed field, that is less than 0.5 °C of the mean surface temperature within a 4 km by 4 km region centered on the fallowed field (see Methods). In general, we find these reference locations to be at least 500m away from the center of the fallow field (Fig. 2a; Fig. S5). Across all fallowed lands in the Central Valley, we find that the fallowed heat island results in up to 4°C changes in surface temperature of nearby consecutively connected agricultural croplands and that the heat from the fallowed lands radiate outward (magenta line in Fig. 2b). We also find that this heat dissipation, away from the fallowed land, is largely exponential, indicating a stronger initial decrease in surface temperature and a gradual one thereafter. Specifically, within the first 200 m, the heat decreased by approximately 3.5 °C away from the fallowed field and by less than 0.5 °C for the next 300 m. In other words, after 200 m, the fallowed heat island intensity decreased by approximately 88% from its peak (about 62% in the first 100 m), adjacent to the fallow land. This gradual decline in heat away from the fallowed center is similar to those found for major cities due to urban heat island (45). Furthermore, we determine how much additional heat is added by the fallowed heat island over the background temperature, by estimating the intensity of the fallowed heat island relative to the mean surface temperature when non-fallowed agricultural croplands replace the fallowed land (cyan in Fig. 2b). We find that the fallowed heat island effects add considerable heat above the background temperature, with the maximum impacts next to the fallowed land and decreasing away, as with the intensity of fallowed heat island (ΔT).

While the fallowed heat island effects substantially increase the temperature of the surrounding croplands, this temperature increase also depends on several factors, including the region, area size, and the extent of surface bareness of the fallow lands. First, we find that the fallowed heat island intensity (ΔT) for the hot-temperate region of the southern San Joaquin Valley (R1; 4.5°C) is approximately 1°C higher than that of the cool-temperate region of the northern San Joaquin Valley (R2; 3.3°C) and the northern Sacramento Valley (R3; 3.8°C; Fig. 2c). Second, we find that the intensity of fallowed heat islands increases as a function of the area coverage of the fallow lands. Specifically, the intensity of the fallowed heat island is up to about 3°C for smaller fallowed land areas (< 10 pixels or ~9,000 m^2), whereas it is up to about 5°C for the larger fallowed land area exceeding ~90,000 m^2 (Fig. 2d). In addition, the relative heat accounted by the fallowed heat island

effect follow similar dissipation rates as the intensity largely because of the similarly in the background surface temperature when averaged across the Central Valley (compare Fig. 2d with Fig. S6b & e). Third, given that there is a degree of variability in the exposure of the fallowed lands (Fig. S3; Fig. S4b), we find that the fallowed heat island intensity with bare surfaces ($B \geq 0.8$) reaches up to 6 °C (17% relative heat) and stronger by about 2 °C (12% relative heat) and 4.5 °C (4% relative heat) more than sparsely vegetated ($0.6 \leq B < 0.8$) or vegetated surfaces ($B < 0.6$), respectively (compare Fig. 2e with Fig. S6c & f). These results suggest that surface bareness of the fallowed lands amplifies the fallowed heat island effect with higher impacts when the fallowed land area is larger. In addition, we also find that the crop types of the nearby cropland likely influence the spatial extent of the heat induced by the fallowed heat island (Fig. S7). To address this, we classify the crop types into similar groups (see Table S1), and we find that the Deciduous Fruits and Nuts (such as grapes and almonds), and Corn and Cotton have the highest heat island intensity of up to 3.1°C near the fallowed center (Fig. S7b). In contrast, Citrus and Subtropical, Truck Crops, and Field Crops display much weaker intensity, generally below 1.5°C. Our result suggests that the differences in planting density coverage, canopy structure, and irrigation methods influence the amount of heat absorbed by nearby croplands. Overall, our findings indicate that the fallowed heat island effect depends sensitively on the fallow location or latitude, area size, and the extent of surface exposure, as well as the crop type of the nearby irrigated croplands.

Effect of Fallowed Heat Island on Water Demand:

As a result of the fallowed heat island effect, we find that the heat dissipated by fallowed land substantially impacts the evapotranspiration and water demand for optimal growth of nearby agricultural croplands. To show the effect of the heat island on nearby evapotranspiration, we obtained 30m-resolution pixel evapotranspiration (ET) data from the OpenET project (46) and estimated the changes in evapotranspiration of nearby agricultural croplands surrounding fallowed lands (see Methods). There is a significant change in evapotranspiration, creating an inverted cone-like structure which varies away from the centralized fallowed locations (Fig. S8). Specifically, we find lower evapotranspiration at the surrounding agricultural croplands near the fallow locations compared to those farther away (Fig. S8). Estimating the change in evapotranspiration (ΔET), similar to the fallowed heat island intensity, we find an evapotranspiration deficit up to -29 mm close to the fallowed locations when averaged across the Central Valley (compare Fig. 3a and Fig. 2b). This reduction is relative to a reference location, which is the maximum evapotranspiration at a distance greater than 500m away from the fallowed land, defined by the fallowed heat island (cf. Fig. 2; see Methods). Like heat dissipation, the evapotranspiration deficit also exponentially decreases (mean evapotranspiration increases) away from the centralized fallowed lands, recovering by about 84 % within the first 200 m (about 65 % within the first 100 m). Overall, the reduction in evapotranspiration around the fallowed land suggests soil moisture deficits resulting from the significant increase in surface temperature due to the fallowed heat island effect.

Accordingly, we estimate the relative water demand (or need) associated with the evapotranspiration and soil moisture deficit by assuming that crop and total evapotranspiration are proportional and that the effective precipitation reaching the crop root, including the

precipitation, run-offs, nominal irrigation, and deep percolation, is constant (see Methods). Specifically, we take the relative water demand as indicative of the total water lost through soil evaporation and plant transpiration required for the crop to reach its full production potential or optimal growth under ideal conditions. Therefore, we estimate the relative water demand as the relative percentage of the evapotranspiration deficit (ΔET) due to the fallowed heat island effect per unit change in the baseline evapotranspiration when the fallowed land is replaced by non-fallowed cropland (see Methods). The results indicate that the fallowed heat island effect accounts for up to 19% of the additional water demand for optimal growth near the fallowed locations, when compared against cases with non-fallowed croplands, across the Central Valley (cyan line in Fig. 3a). In addition, the increase in water demand also depends on the region of the fallowed locations, the size of the fallowed area, how exposed the fallowed land is, and the crop type (Fig. 3b-d), which corresponds to a similar reduction in evapotranspiration due to the fallowed heat island effect (Fig. S9 and Fig. S10). Depending on the region, size of the fallowed area, and surface bareness, this fallowed heat island effect could account for up to ~40% of additional water demand (Fig. 3b-d), corresponding to almost -60 mm deficit in evapotranspiration, near the fallowed locations (Fig. S9). These water demands are largely proportional to the temperature intensity change around the farmed lands (compare Fig. 3b-d with Fig. 2c-e), suggesting that warmer surface temperatures lead to a higher vapor pressure deficit in the air, causing plants to lose more water through transpiration and the soil to lose more water through evaporation. In addition, the water demand also depends on the crop type and category, where the fallowed heat island effect requires up to 20 % and 12 % of additional water demand for deciduous fruits and nuts, and corn and cotton, respectively near the fallowed locations across the Central Valley, higher than other crop type, such as citrus and subtropical (Fig. S10). Due to the relatively lower surface temperature resulting from the fallowed heat island effect, other crop categories, including field crops, grains, berries, and citrus, require relatively less additional water demand. Overall, our findings indicate that the fallowed heat island effect results in a substantial deficit in evapotranspiration and water demand, which varies by region, fallow size, and surface bareness, with the maximum effect occurring near the fallowed locations and decreasing exponentially with distance.

Effect of Fallowed Heat Island on Crop Yield:

The co-occurrence of warmer surface temperatures and reduced evapotranspiration, or higher water demand due to the fallowed heat island effects, also alters crop yields of nearby cropland to the fallowed lands. Our results above suggest that warmer surface temperatures generally have a negative correlation with lower evapotranspiration, and joint probability analysis further confirms that this general co-occurrence is more likely (54%) at temperatures higher than 50 ^{o}C and evapotranspiration less than 50 mm over fallowed locations (Fig. S11a). However, not all fallowed lands have this negative correlation between surface temperature and evapotranspiration (Fig. S11b), suggesting that both temperature and moisture perturbations can influence crop yield and productivity through different pathways near the fallow locations. Therefore, to estimate the impacts of fallowed heat island effect on crop yield, we consider the temperature-evapotranspiration coupling (47, 48) rather than only the temperature, which is often used in simple linear regression by some previous studies (49, 50) (e.g., Fig. S12). We do so because previous studies

showed that in regions where temperature and moisture are strongly coupled, crop yields are more negatively affected by warming, as moisture deficits often accompany heat stress (48). To account for the impacts of temperature-evapotranspiration coupling due to the fallowed heat island effect on the crop yield, we focus on three major crops over the California Central Valley (cotton, corn, and tomato) and estimate the response of crop yield sensitivity to the temperature-evapotranspiration coupling over the adjacent cropland to the fallowed center (see Method). These crops collectively account for 17% of the total cropland area in the Central Valley, resulting in an average yield of 27, 0.87, and 56 tons per acre for Corn, Cotton, and Tomatoes, respectively, between 2013 and 2022 (Fig. S12 & S13). We employed a new framework, following Lesk et al. (202), to estimate the relative change in crop yield due to the fallowed heat island effect (see Methods).

We find that, when accounting for the temperature-moisture coupling, there is a significant difference in the fallowed heat island effects on crop yield, leading to a mean reduction of up to 2.6% above the baseline crop yield when averaged across the three crops (Fig. 4a). Specifically, the fallowed heat island effect accounts for up to 5.3%, 1.8%, and 0.6% reduction in yield for corn, cotton, and tomatoes above the mean baseline (Fig. 4a; cf. Fig. S14). Most of the relative reduction in crop yield occurs in the first 100 m away from the fallowed land, which follows a similar pattern of reduction in the relative heat and water demand (Fig. 4a & Fig. S15). On average, for the first 100 m, the relative reduction in crop yield is -2.1%. -1.1%, and -0.2% for corn, cotton, and tomatoes of the mean baseline (first column in Fig. 4b). In addition, the reduction in relative crop yields due to the fallowed heat island effects also varies across regions and counties in the Central Valley. Specifically, on average, regions with warmer surface temperature (R1 & R2) have the largest reduction in relative crop yield (-1.0 % & - 1.6 %) across the three crops when averaged for the first 100 m away from the fallowed lands than regions with cooler surface temperature (R3) with smaller reduction (-0.8%; Fig. 4b). For individual crop, this difference in crop yield of the same crop across the regions could be up to an order of magnitude (Fig. 4b). Within each region, there is also differences in the percentage reduction in relative yield impacts. For example, Tulare County in San Joaquin Valley consistently have the largest reduction in relative crop yield impacts across the three crops, despite not having the largest surface temperature or fallowed land coverage (compare Fig. S16 and S1 to Fig. 1). In contrast, Kern County have the highest surface temperature and fallowed land coverage, but relatively less reduction in relative crop yield impacts compared to Tulare County. This difference between the percentage change in crop yield of the crop types across counties is partly due to the response of yield sensitivity for each crop to temperature-moisture coupling and the crop-specific relative heat impacts due to the fallowed heat island (Fig. 4c & d). For example, the response of crop yield sensitivity to temperature-moisture coupling is stronger for corn and tomatoes than for cotton, which is more sensitive to the direct relative heat impacts due to fallowed heat island (Fig. 4c & d). Overall, between and within regions in the Central Valley, there are significant reductions in the relative impacts of the fallowed heat island effect on crop yield for corn, cotton, and tomatoes, highlighting a critical and spatially variable pathway through which land management decisions, such as fallowing, often affect agricultural productivity.

Discussion

We have shown that the fallowed heat island, a phenomenon defined similarly as urban heat island, whereby exposed fallowed lands in agricultural areas absorb intense solar radiation resulting in significantly higher surface temperature than do its surrounding croplands, is frequently induced in California Central Valley (Fig. 5). Specifically, we showed that the fallowed heat island effect raise the surface temperature of nearby agricultural lands by as much as 6°C and create a cone-like structure that radially spreads heat outwards away from the fallowed locations. In addition, we also showed that this fallowed heat island effect is associated with evapotranspiration deficit of up to -60 mm, corresponding to almost 40% additional water demand over the adjacent agricultural croplands. Consequently, because of the higher surface temperature and evapotranspiration deficit in adjacent croplands, we find a reduction in relative crop yield for nearby corn, cotton, and tomato of up to 5.3%, 1.8%, and 0.6% % (mean of 2.6%), respectively, when compared to the county-level baselines. Furthermore, we showed that the intensity of the fallowed heat island depends on the latitudinal region of the fallowed lands, the overall coverage size of the fallowed area, the degree of surface exposure of the fallowed land (measured by bareness), and the type of crops planted next to the fallowed land areas. Specifically, we showed that (1) the intensity is stronger for fallowed lands in the southern part of Central Valley, where the mean surface temperature is generally higher (the San Joaquin region) than the northern part, where the mean surface temperature is cooler (the Sacramento Valley); (2) the intensity is stronger for larger cluster of fallowed lands with increased exposed surface area to absorbed solar radiation than smaller fallowed fields; (3) the intensity is stronger when the fallowed surfaces are bare and exposed to solar radiation increasing the ability to absorb heat than to when they are sparsely covered by vegetation; (4) finally, the intensity is stronger for some crops planted adjacent to the fallowed lands than others, suggesting that planting density coverage, canopy structure, and irrigation methods influence the amount of heat absorbed by nearby croplands. Consequently, these variations in the intensity of fallowed heat island also inform similar variations in relative water demand and relative crop yields.

Our findings that highlight the effects of fallowed heat island contrast with the mechanism of irrigation cooling effects in agricultural lands. Previous studies have shown that cooling effects between irrigated and adjacent non-irrigated areas could be more than 6 °C during the growing season in arid and semiarid areas (51). This temperature change due to irrigation cooling effect is similar but opposite to our results of increased surface temperature of up to 6°C due to fallowed heat island (see Fig. 2). This suggests that the irrigation cooling effect operates through the similar fundamental energy balance mechanisms that drive our observed fallowed heat island, but in reverse. Whereas irrigation cooling acts through increases in evapotranspiration, shifting the energy budget toward latent heat flux, thereby lowering land surface temperature, fallowed heat island effects amplify surface warming and reduce evapotranspiration through increased sensible heat flux and reduced latent heat flux (52, 53). In addition, the spatial patterns of these contrasting effects also share similar distance-decay relationships, with maximum effects occurring at the source and diminishing exponentially outward (54, 55), similar to urban heat island (56). While the negative

effects of fallowed heat island effect can be counteracted by enhanced irrigation, our findings suggest that strategies that maximize cooling through irrigation must be balanced against strategies that conserve water via fallowing.

In addition, our findings have other important implications. First, the enhanced surface temperature and soil moisture deficits resulting from fallowed heat islands can influence soil carbon sequestration and soil fertility, particularly in nearby agricultural fields (1). Specifically, an increased surface temperature exacerbating soil moisture deficit can increase the rate at which soil microorganisms decompose organic matter, resulting in increased carbon dioxide release into the atmosphere and a decrease in the amount of carbon stored in the soil (57–59). Second, enhanced surface temperature due to the fallowed heat island can also affect livestock, particularly dairy cows, which are vulnerable to heat stress. Specifically, cows may be susceptible to additional heat stress near fallowed lands, which can reduce feed intake, milk production, and reproductive success (60). Third, fallowed heat island effects could further influence the local microclimates, which could have potential consequences for air quality and the health of farmworkers, especially in regions with increasing climate-induced features such as drought and heatwaves. These potential consequences for the health of farmworkers contrast with the influence of irrigation cooling (61). Specifically, enhanced localized heat sources such as those from fallowed lands could induce changes in the pressure gradients that could affect the wind distribution and direction (62). Such changes in wind could further result in the redistribution of the relative heat impacts on nearby croplands. In addition, the coupling between temperature-bareness over fallowed land (e.g., Fig. S4) has previously been associated with increased potential for dust emission and mobilization, which changes in wind direction could exacerbate. The combined effects of enhanced temperature and secondary effects through dust mobilization could exacerbate health and air quality hazards, increasing occupational heat exposure risks for farmworkers in and around these agricultural fields (63).

Despite the impacts of these fallowed heat island effects on the surrounding croplands, there are some potential limitations and caveats that should be considered in interpreting our results. First, our study relies on satellite-based surface temperature, surface bareness, and evapotranspiration that may be associated with inherent uncertainties in their retrieval procedures (64–66). For example, Landsat-8 retrievals of surface reflectance in relevant bands could have outliers that may propagate into our estimate, resulting in a higher surface temperature than physically possible (67). Such uncertainties are mitigated in our study by averaging millions of data points over multiple years and locations across the Central Valley. Second, in addition to uncertainties in satellite-based products, our Landsat-8 surface temperature and surface bareness information rely on monthly averages that are obtained from about two Landsat overpasses due to the long return time. Because of the difficulty of capturing daily variability in the monthly averages, our estimates are slightly biased-high in some places and biased-low in others. That said, we expect that the contribution of this bias to the overall uncertainties to be less than others because daily mean surface temperature and bareness, within a given month, do not change significantly and generally within 5% of the monthly averages, between June and August in the Central Valley. Third, the fallowed land information from USDA's Cropland Data Layer (CDL) is only available

yearly, and seasonal comparisons between fallowed land and other variables, such as surface temperature, surface bareness, and evapotranspiration, were not possible. However, CDL's fallowed land cover information is often obtained for the previous-year growing season (68), which corresponds, in part, to the period considered in our study (June-August). Fourth, there are additional uncertainties potentially introduced in our analysis of the surface temperature over the 780 m × 780 m regions surrounding a centered fallowed area. Specifically, because of the spatial variability and heterogeneity in local land cover and geographic features, agricultural croplands may be randomly interspersed with fallowed lands of different sizes (Fig. S14), thus making it difficult to determine exactly which fallowed land has the most influence on nearby cropland. Additionally, even when non-fallowed non-agricultural land cover types have been excluded from our analysis (see Table S2), it is difficult to mitigate their impacts on surrounding agricultural croplands that are eventually used in our analysis. To account for this bias, we required that the centered fallowed locations be followed by consecutively connected agricultural croplands, which we implemented only across possible directions. While this approach minimizes the influence of other non-fallowed non-crop land cover, it also reduces the number of data points in the estimate of the fallowed heat island intensity and its relative impacts. Finally, although annual crop yield information is used to estimate the impacts of the fallowed heat island, they are compared against the influence of surface temperature and evapotranspiration between June and August. Since our study is only concerned about co-variabilities in surface temperature, evapotranspiration, and crop yield in estimating the relative impact of the fallowed heat island on crop yield, we assume that such variabilities will be proportional whether an annual or a limited period is taken during the growing season. We also assume that other factors that may have an impact on the crop yield remain constant, including climatic and environmental factors, such as precipitation, soil moisture, heat waves, as well as others that influence crop production, such as the use of pesticides, insecticides, fertilizers, and so on. While this may introduce uncertainties in the magnitude of the relative change in crop yield, the general reduction in crop yields due to the fallowed heat island will remain the same.

Despite these limitations, our findings provide strong evidence of changes in surface temperature near fallowed lands, inducing the fallowed heat island effects, with impacts on water demand and crop yield of the adjacent agricultural fields. As such, our study provides a new lens on how land management can amplify local climate extremes and unintentionally affect surrounding crop systems. Considering the potential effects of the fallowed heat island in agricultural planning, possibly by clustering fallowed fields, maintaining vegetative buffers, or leveraging cover crops, could help mitigate its unintended negative impacts and consequences. In addition, our study underscores the importance of considering land-use externalities in agricultural water management strategies, particularly those associated with the Sustainable Groundwater Management Act (SGMA). While land fallowing is often a necessary response to drought and resource limitations, its unintended side effects may offset some of the intended benefits by imposing thermal stress on adjacent productive croplands. These effects are particularly concerning given the scale of fallowing observed in recent years in the Central Valley (17) and the projected increase in such practices due to changing water availability and policy shifts in California (26). Taken together, our study suggests that continued expansion of fallowed lands may further amplify the fallowed heat

island effects in the Central Valley, with potentially cascading impacts on agricultural productivity and public health. Without targeted mitigation efforts, the fallowed heat island effects are likely to intensify in a warming climate.

Materials and Methods

Our study examines the difference in surface temperature between fallowed lands and other actively cultivated nearby croplands and how fallowed lands influence evapotranspiration, water demand, and crop yield of the nearby agricultural fields. To understand these impacts, we focused on the California Central Valley, a major U.S. agricultural region, covering the Sacramento Valley in the northern parts and the San Joaquin Valley in the southern parts (Fig. 1). In addition, we focus on the period between June and August, when temperatures are highest (Fig. S17 & Fig. S1). Although this period is often associated with little to no direct rainfall (69), it is also part of the primary growing season during which agricultural productivity is maintained through active irrigation (69). We obtained surface temperature, evapotranspiration, and crop yield information between June and August for a 10-year period, from 2013 to 2022, which is sufficient to capture interannual variability and reduce uncertainties in our estimates of the fallowed heat island effects.
Below, we detail our methodology, which leveraged multiple observational and remotely sensed products at 30-m resolution. These include remotely sensed observational datasets for cropland classification and land cover type identification, as well as for estimating land surface temperature, surface bareness, and evapotranspiration.

Identifying Fallowed and Non-Fallowed Agricultural Lands:

Information about fallowed and non-fallowed agricultural lands was obtained from the Cropland Data Layer (CDL) products produced by the National Agricultural Statistics Service (NASS) of the U.S. Department of Agriculture (USDA). The CDL is an annual high-resolution (30m) crop-specific, georeferenced, raster-formatted land cover map created by a combination of satellite imagery, ground truth data, and other auxiliary data, such as the National Land Cover Data Collection (41). Specifically, the USDA integrates both cultivated and fallow croplands into the CDL products by utilizing crop acreage data reported by the USDA Farm Service Agency (FSA) for accuracy assessment and crop classification training (19). While the CDL remains one of the most comprehensive datasets for agricultural land cover in the United States, certain uncertainties persist due to its reliance on satellite remote sensing. These uncertainties include its limitation to land cover (rather than land use) identification, pixel-level classification that may introduce spatial bias, and potential classification errors associated with spectral similarity among classes (71). Despite these limitations, the CDL remains one of the most reliable and consistent sources of land cover information for crop classification available for the Contiguous United States (41).
In this study, we defined fallowed and non-fallowed croplands based on CDL's crop types and land cover classification. Fallowed lands were identified from the CDL category labeled "Fallow/Idle Cropland" (41). In addition, we also categorized the non-fallowed crop types into broad classes based on the classification scheme outlined in (17), including Citrus & Subtropical, Deciduous Fruits & Nuts, Double Field & Grain, Field Crops, Grain & Hay, Truck Crops & Berries (see Table S1). The areas and locations identified by these crop types are generally referred to as croplands or agricultural lands in the main text, and

they represent the areas around the fallowed lands (see below). Consequently, we excluded certain non-crop and non-fallow land cover types, including Open Space, Wetlands, Barren, Perennial Ice/Snow, Urban, and various Forests and Shrublands from our analysis to limit potential uncertainties in our assessment of the fallowed heat island effect and to ensure the focus remained on agricultural regions surrounding the fallowed locations (see Table S2). Furthermore, because fallowed locations do not always occur as an isolated 30 m × 30 m single-pixel, we developed a framework to identify connected fallowed areas to determine the impact of fallowed area size on the fallowed heat island effect (cf. Fig. 2 & 3). Specifically, we define larger fallowed areas as consisting of contiguous clusters of connected 30-m-resolution fallowed pixels and separated from any other nearby cluster or isolated fallowed field by at least one pixel of non-fallowed land cover type (e.g., crop type). An example of different fallowed land area sizes is shown in Figure S18, taken over an area in Kern County, with different colors indicating different fallowed area sizes. Overall, all fallowed land and non-fallowed cropland pixels are shown in Figures 1a and S1, which indicate higher density in the Central Valley compared to other regions in California. The highest fallowed areas are found in Kern (875 km^2), Fresno (827 km^2), and Kings (685 km^2) counties in southern part of San Joaquin Valley; Sacramento (106 km^2), San Joaquin (73 km^2), and Stanislaus (24 km^2) counties in northern part of San Joaquin and southern part of Sacramento Valley; and Sutter (300 km^2), Yolo (294 km^2), and Colusa (291 km^2) counties in northern part of Sacramento Valley (Fig. S1). These fallowed land coverage peaks at approximately 45% of the total croplands in some counties of the San Joaquin and Sacramento Valleys regions of the Central Valley (Fig. 1d).

Obtaining Satellite-derived Surface Temperature and Bareness:

We obtained surface temperature and surface bareness leveraging monthly surface reflectance from Landsat-8 between July and August 2013 and 2022 (43). Launched in February 2013 with operational capabilities from March 2013 (42). Landsat-8 was equipped with two sensors, Operational Land Imager (OLI) and Thermal Infrared Sensor (TIRS), which operate in the thermal infrared band and are used to estimate land surface temperature (72). The TIRS thermal band has a native resolution of 100 m, which is downscaled to 30 m in the final Landsat product to match the spatial resolution of the reflective bands (73). We used Landsat-8 due to its superior spatial resolution and advanced sensor capabilities, including better signal-to-noise characteristics and higher radiometric resolution (74), resulting in higher-quality datasets compared to previous-generation Landsat-7 (75, 76). In addition, although Landsat-9 has similar sensors to Landsat-8, it only became operational at the end of 2021. Therefore, we ignore Landsat-9 in this study because it does not cover our period of interest, and to avoid potential inconsistencies that may introduce errors into our estimates by combining both Landsat-8 and Landsat-9. We use the publicly available Landsat-8 level 2 collection 2 Tier 1 repository (77) accessed through the cloud-based Google Earth Engine platform (78). These imageries are provided at a spatial resolution of 30 meters and at a temporal interval of 16 days, with the overpass time between 10 am and 10:40 am local time, meaning each location is revisited approximately twice per month (72). Effectively, we took the average over each location and used the monthly values between June and August, 2013-2022.

We first obtain the monthly Normalized Difference Vegetation Index (NDVI) from Landsat-8 using the red and near-infrared (NIR) bands, which correspond to Surface Reflectance (SR) bands 4 (SR_4) and 5 (SR_5), respectively (42).

$$NDVI = {SR_5(NIR) - SR_4(RED)}\Big/{SR_5(NIR) + SR_4(RED)} \quad (1)$$

The above equation suggests that higher NDVI values are areas of denser or healthier vegetation that strongly reflect near-infrared radiation while absorbing more visible red light. Because we are concerned with the exposure of fallowed land surfaces, we estimated instead the surface bareness (B), following Pu & Ginoux, (2017), as:

$$B = e^{-NDVI} \quad (2)$$

This expression indicates that B is always greater than 0 and allows us to better capture small variations in surface characteristics. Given the distribution of surface bareness for fallowed land surfaces (top part of Fig. S4b), we classify B into four categories: "vegetated" (B < 0.6), "sparsely vegetated" (0.6 ≤ B < 0.8), "moderately bare" (0.8 ≤ B < 0.9), and "totally bare" (B ≥ 0.9). Where necessary, bare surfaces are simply represented by B > 0.8. By categorizing bareness into these four groups, we aimed to capture how different types of fallowed land surfaces influence surface temperature variations, and consequently the fallowed heat island effects.

To obtain land surface temperature (T) from Landsat-8, we leveraged NDVI obtained above (Eq. 1) and followed a similar method used in previous studies, such as Avdan & Jovanovska (2016), An et al. (2022) and Faqe Ibrahim (2017) to obtain the parameters needed to estimate the land surface temperature (T):

$$T = {BT}\Big/{1 + \left(\frac{\lambda \cdot BT}{\rho}\right) ln\varepsilon} \quad (3)$$

Where $\lambda = 10.895\ \mu m$ is the wavelength at the center of the emitted radiance of band 10, $\rho = \frac{hc}{\sigma} = 1.438\ x\ 10^{-2}\ mK$ is a constant value (because σ is the Boltzmann constant, 1.38 × 10−23 J/K, h is Planck's constant, 6.626 × 10−34 J s, and c is the velocity of light, 2.998 × 10^8 m/s; representing the radiation constant derived from Planck's law, essential for the emissivity correction in land surface temperature retrieval (83), and $\varepsilon = 0.004 \times FV + 0.986$ is the spectral emissivity. The 0.004 coefficient represents the emissivity variation due to vegetation, while the 0.986 corresponds to the baseline soil emissivity including a surface roughness correction (84). $FV = \left(\frac{NDVI - NDVI_{min}}{(NDVI_{max} - NDVI_{min}}\right)^2$ represents the fraction of vegetation, and it is used to assess the relative amount of vegetation in a given area based on NDVI values. It offers important information about land cover and ecosystem conditions, with higher FV values representing a greater vegetation presence (85). BT in Equation 3 is the at-sensor brightness temperature, ST_B10 band 10, which is defined as the surface temperature band in Landsat-8 as a digital number (DN). To convert DN into a physically meaningful variable, the DN is multiplied by the scale factor and added to the offset provided in the metadata, as described in the Landsat-8 user guide (42, 72), $BT = (DN \times 0.00341802) + 149.0$ where BT is in Kelvin (K). To ensure data quality, we masked cloud and cloud-shadow affected pixels using the Quality Assessment (QA_PIXEL) band. Following the USGS bitmask definition, pixels with cloud (bit 3 = 1) or cloud shadow (bit 4 = 1) flags were excluded, and only pixels with both flags equal to zero were retained (42). After applying these masks, we generated a median composite for

the study period (June–August) and clipped the imagery to the area of interest. Finally, we converted BT and consequently T from Kelvin (K) to Celsius (◦C).

Estimating Fallowed Heat Island Intensity and the Relative Heat Impacts:
We use the land surface temperature (T) above to determine the change in temperature or intensity (ΔT) due to the fallowed heat island effect. To do so, we first obtain the surface temperature of the surrounding cropland centered on the fallowed lands identified across the Central Valley. Specifically, we defined the surrounding area around a fallow land by considering approximately 800 m, in all directions (north, south, east, and west) of the fallowed land (see Fig. 2 and Fig. S8). In addition, we require that the surrounding cropland pixels to be all actively cropland pixels with defined crop types based on classification from CDL (see Table S1). Because agricultural croplands are often randomly interspersed with fallowed lands of different sizes (e.g., Fig. S18), it is difficult to determine exactly which fallowed land has the most influence on a nearby cropland. Therefore, we further require that the centered fallowed location be followed by consecutively connected agricultural croplands within the 780-m × 780-m area. To accomplish this, we iterate across all directions from the fallowed center and only retain directions with consecutively connected agricultural pixels for the entire 780 m. While this approach is easily applied for an isolated fallowed pixel at the center of the 780-m x 780-m area (Fig. S19a), it creates a challenge for fallowed pixels that are often part of a larger fallowed cluster (Fig. S19). For these latter cases, we take the outermost fallowed pixels around the boundary of the fallowed cluster as the "centered fallowed pixel" and similarly retain consecutively connected agricultural croplands along possible directions away from it (Fig. S19b). In doing so, we assume that other non-fallowed non-agricultural land cover types, although excluded (see Table S2) do not have impacts on surrounding agricultural croplands that are eventually used in our analysis. Overall, this approach allowed us to evaluate the spatial propagation of thermal influence away from fallowed lands into adjacent agricultural regions.
Consequently, we estimated the fallowed heat island intensity (ΔT; Fig. 2b) as the difference between the land surface temperature of the consecutively connected agricultural pixels surrounding and influenced by the fallowed center (T_{FHI}) and a reference land surface temperature far away from the fallowed center (T_{REF}). That is:

$$\Delta T\ (x, y) = T_{FHI}(x, y) - T_{REF} \quad (4)$$

Where we obtain $\Delta T\ (x, y)$ and $T_{FHI}(x, y)$ at locations x, y, within the 780-m × 780-m area near the fallowed lands. In addition, we define T_{REF} over the location of the first minimum surface temperature, away from the fallowed center, that is less than 0.5 °C of the mean surface temperature within a 4 km by 4 km region. We use a larger region for T_{REF} to ensure that the mean regional temperature that is not influenced by the fallowed land is obtained as the reference temperature. This approach is conceptually similar to how previous studies estimate the intensity of the urban heat island effect, where the reference temperature is often taken at a rural or suburban region far from the city center (4, 86, 87). In general, we find T_{REF} at locations at least 500m away from the center of the fallow field across the different regions of the Central Valley.

In addition, we obtain the relative heat impacts (*RHI*) of the fallowed heat island by estimating the contribution of the intensity, ΔT, relative to the baseline surface temperature that the location would have if not affected by the fallowed heat island effect.

$$RHI\ (\%) = \left[{\Delta T\ (x,y)}\Big/{T_{NFL}(x,y)}\right] \times 100 \quad (5)$$

Where T_{NFL} surface temperature over the same locations for years when the target central pixel was non-fallow land (NFL) and similarly surrounded by consecutively connected agricultural pixels at locations x, y, within the 780-m × 780-m area.

In equation (5), we assume that surface temperature can be used as a proxy for near-surface air temperature such that the relative heat impact (RHI) reflects the direct thermal influence of the land surface on surrounding cropland. While the surface temperature and air temperature are not strictly proportional, previous studies show they are often correlated, with the relationship depending on land cover, surface moisture, and atmospheric conditions (88–90). Thus, using surface temperature as a proxy provides a reasonable first-order estimate of the thermal stress imposed by the fallowed heat island.

Estimating the Fallowed Heat Island Effects on Evapotranspiration and Water Demand:

Similar to the fallowed heat island intensity and relative heat impacts, we estimated the effect of fallowed heat island on evapotranspiration (ΔET) and relative water demand (RWD) using evapotranspiration information from the OpenET project (Fig. 4 & Fig. S7 & S8). The OpenET project is a collaborative effort that delivers satellite-based evapotranspiration estimates across the Contiguous United States (44). It integrates multiple satellite-driven models to provide spatially and temporally consistent evapotranspiration information at a 30-meter resolution, suitable to evaluate field-scale water use patterns in agricultural lands (91). In addition, this dataset provides a single "ensemble value" using the mean from six evapotranspiration models, including ALEXI/DisALEXI, eeMETRIC, geeSEBAL, PT-JPL, SIMS, and SSEBop, which are all implemented on the Google Earth Engine platform with a monthly temporal resolution (78, 92, 93). Specifically, the ensemble values are determined after applying a filtering process that eliminates outliers, utilizing the median absolute deviation method. We obtained the evapotranspiration for the same months and locations as the land surface temperature from the Landsat-8. The relationship between evapotranspiration and land surface temperature is important in semi-arid and arid regions, where reduced evapotranspiration can lead to higher surface temperatures due to decreased latent heat flux (94). Where fallowed lands are prevalent, they could disrupt local evapotranspiration patterns by reducing transpiration from crops while increasing evaporation from bare soil, potentially leading to localized warming and changes in moisture availability (95).

We estimated the fallowed heat island effect on evapotranspiration (ΔET; Fig. 3) as the difference between the evapotranspiration of the consecutively connected agricultural pixels surrounding and influenced by the fallowed lands (ET_{FHI}) and a reference evapotranspiration far away from the fallowed center (ET_{REF}), following equation 4 above. Like T_{REF}, ET_{REF} is the maximum evapotranspiration at a distance greater than 500m away from the fallowed land, defined by T_{REF} (see Eqn. 4 above).

$$\Delta ET(x,y) = ET_{FHI}(x,y) - ET_{REF} \quad (6)$$

In addition, we use the estimates of change in evapotranspiration (ΔET) to estimate the relative water demand by the nearby region affected by the fallowed heat island effect. To do so, we first determine the crop requirement or the water deficit (WD) using the water-

balance approach, whereby WD is the amount of water required for optimal growth of a crop, following the Food and Agriculture Organization (FAO) (96):

$$WD = ET_c - P_e \quad (7)$$

Where P_e is the effective precipitation available to the soil, which depends on the total precipitation (P), nominal irrigation (Irr), runoffs (R), evaporation (E) and deep percolation (D_p) (96–98); that is $\mathrm{P_e} \approx P + Irr - R - E - D_p$) ; ET_c is the crop evapotranspiration, which depends on the reference evapotranspiration (ET_o; the water loss from a reference surface, like grass, under specific weather conditions and can be estimated using based on the Penman–Monteith method; (99) and the crop coefficient (K_c; a factor that adjusts ET_c to reflect the water use of a specific crop at different growth stages): $ET_c = ET_o \cdot K_c$. To estimate the relative water deficit, we assume that crop evapotranspiration (ET_c) is proportional to the total evapotranspiration ($ET \propto ET_c$), given the high correlation between temperature and evapotranspiration (Fig. S11). In addition, we also assume that the effective precipitation available to the soil is unchanged within the 4-km x 4-km, such that the P_e close the fallow land and those far away are the same, for a given crop type during the growing season. Given that there is little to no precipitation and available water to crops through irrigation does not change during the growing season in the Central Valley, we estimate that this assumption has no significant influence on our results. Therefore, we obtain the relative water deficit (RWD) by estimating the contribution of the evaporation deficit affected by the fallowed lands (ΔET) relative to the baseline evapotranspiration that the location would have if not affected by the fallowed heat island effect ($\mathrm{ET_{NFL}}$), following equation 5, that is:

$$RWD\ (\%) = \left[\Delta WD \big/ WD_{NFL}\right] \approx \left[\Delta ET(x,y) \big/ ET_{NFL}(x,y)\right] \times 100 \quad (8)$$

In the results section, we present the relative water demand, which is the opposite of the relative water deficit, achieved by simply multiplying RIWD by -1.

Estimating the Sensitivities of the Fallowed Heat Island Effects:

We further separate the effects of the fallowed heat island on the intensity (ΔT), relative heat impact (RHI), evapotranspiration (ΔET), and relative water demand (RWD) as a function of region where the fallowed lands are located, the fallowed area sizes, and surface bareness (B) of the fallowed lands, and the dominant crop type surrounding the fallow lands. First, given the latitudinal variations of surface temperature in the Central Valley, from the semi-arid south to the temperate north, we separate the counties in three regions (see Fig. 1e and Fig. S1), including the southern part the San Joaquin Valley (R1; comprising of Kern, Kings, Tulare, Fresno and Madera), the northern part of San Joaquin Valley and Metro Sacramento (R2; comprising of Merced, San Joaquin, Stanislaus, and Sacramento), and the northern part of Sacramento Valley (R3; comprising of Sutter, Yolo, Colusa, Glenn, Yuba, Butte, Tehama). The R1 region has the highest fallowed land coverage, representing a high percentage of the agricultural croplands, and corresponding to the highest surface temperature compared to the other two regions (compare Fig. 1d, Fig. 1e, and Fig. S1). In addition, the R2 region has the lowest fallowed land coverage representing the lowest percentage of the agricultural croplands than R1 and R3 regions but with similar surface temperature (except for Kern and King counties; see Fig. S1). Second, given the variability in fallowed size areas and the corresponding differences in their averaged surface temperatures that are also region-dependent (Fig. S20), we separated the fallowed land

areas into three categories based on their total area, including fallowed land areas < 9,000 m^2 (<10 pixels; which also include single-pixel 900-m^2 fallowed field); fallowed land areas between 9,000 and 90,000 m^2 (10 - 100 pixels); and fallowed land area > 900,000 m^2 (>100 pixels). While generally the surface temperature of these fallowed lands is roughly similar for the first two classes, they diverge for the largest fallowed size class indicating that larger fallowed areas are hotter, although with relatively fewer numbers (Fig. S20). Third, as shown above, we classified surface bareness (B) into B < 0.6 (vegetated), 0.6 ≤ B < 0.8 (sparsely vegetated), and for the purpose of estimating sensitivities, we combined the bare surfaces as B > 0.8 (bare) surfaces (e.g., Fig. 2e and 3d). Finally, we also considered re-classification of CDL's crop types into six major classes, and estimated their sensitivities to the fallowed heat island, including Citrus & Subtropical, Deciduous Fruits & Nuts, Double Field & Grain, Field Crops, Truck Crops & Berries (see Table S1 & Fig. S7 and S10). In addition, for crop yield estimates, we focused only on three crops: Corn, Cotton, and Tomatoes (see details below; Fig. S15).

Estimating the Fallowed Heat Island Effects on Crop Yield:

Similar to the relative heat impacts and relative water demand, we seek to estimate the relative yield impacts (RYI) due to the fallowed heat island effects on individual crops. Previous studies typically obtain the response of crop yield to increases in temperature using statistical linear regression (35, 100). However, crop yield information is often not available for each crop location or grid point, hence most crop yield responses to temperature are often obtained at a global or regional scale (101), with fine-scale resolution typically at the county-level (101), such as below:

$$\hat{Y}^{c,k}(t) = \hat{\beta}_T^{c,k} T^{c,k}(t) + \epsilon_\beta \quad (9)$$

Where $\hat{\beta}_T^{c,k} = \frac{\partial \hat{Y}^{c,k}}{\partial \mathrm{T^{c,k}}}$ is the response of crop yield, $\hat{Y}^{c,k}$, to crop-specific weighted-average temperature, $T^{c,k}$, for county, k, and crop type, c, over a period, t (Fig. S12); and ϵ_β can be described as the intercept of the regression and other undefined random variables that add noise to the relationship. In the U.S., county-level crop yield information is often obtained from the Department of Agriculture's Agricultural Yield Survey (102), as we do in this study between 2013 and 2022. Here, we focus on annual survey crop yield information for three crops – tomatoes, corn, and cotton – which are among the main crops in California that cover approximately 305 km^2 and account for 17% of the overall cropland coverage across the Central Valley (Fig. S13). In addition, we also focus on these crop types as they are the most complete crop yield information in our criteria, where we required that all counties represented to have at least four years of available crop yield information for regression analysis (see Table S3 and Eqn. 9).

To obtain the crop yield response to temperature due to the fallowed heat island effect at the fine-scale of 30-m by 30-m resolution, we developed a framework that takes into account not only the direct impacts of heat stress on crop yield but also indirect impacts through moisture deficit, following Lesk et al. (2021). We do so because previous studies showed that in regions where temperature and moisture are strongly coupled, crop yields are more negatively affected by warming, as moisture deficits often accompany heat stress (e.g., Fig. S11), creating a feedback process with impacts stronger than considering temperature alone (e.g., Eqn. 9) (103–105). Specifically, we estimated crop yield sensitivity (or crop yield response) to the coupling between heat and moisture deficit, $\Delta\beta^{c,k}(x, y)$, by

assuming that the induced yield response is proportional to the variabilities in the temperature-moisture coupling within the 780-m × 780-m area near the fallowed land and this coupling is modulated by the crop-specific response of the crop yield sensitivity to the coupling (Fig. S21). That is:

$$\Delta\beta^{c,k}(x,y) = \Delta {r_{T,ET}}^{c,k}(x,y) \cdot \hat{\alpha}^{c} \quad (10)$$

Where $\Delta {r_{T,ET}}^{c,k}(x,y)$ is the coupling between temperature and moisture, representing the coupling between heat and water demand, induced by the fallowed heat island effect at locations x, y, near the fallowed lands for each county and each crop type (Fig. S22); and $\hat{\alpha}^{c} = \left(\frac{\partial \hat{\beta}_{T}^{c,k}}{\partial {\hat{r}_{T,ET}}^{c,k}}\right)^{c}$ is the response of crop yield sensitivity, $\hat{\beta}_{T}^{c,k}$ (Eqn. 9 & Fig. S12), to county-specific crop-specific variabilities in the temperature-moisture coupling, ${\hat{r}_{T,ET}}^{c,k}$ (Fig. S23). From Eqn. 10 above, we estimate $\Delta {r_{T,ET}}^{c,k}(x,y)$ as the difference between the mean temperature-evapotranspiration correlations across the county for each crop type and those due to the fallowed heat island effect at locations x, y, near the fallowed lands (Fig. S22). That is:

$$\Delta {r_{T,ET}}^{c,k}(x,y) = {r_{T,ET}}^{c,k}(x,y) - {\hat{r}_{T,ET}}^{c,k} \quad (11)$$

Where ${r_{T,ET}}^{c,k}(x,y) = r[\mathrm{T}^{c,k}(x,y,t), \mathrm{ET}^{c,k}(x,y,t)]$ are the temporal correlations between county-specific crop-specific surface temperature and evapotranspiration due to the fallowed heat island effects at locations x, y, near the fallowed lands (Fig. S24), and ${\hat{r}_{T,ET}}^{c,k} = r[\mathrm{T}^{c,k}(t), \mathrm{ET}^{c,k}(t)]$ is the mean correlation across each county for the specific crop type (Fig. S23). Note that ${\hat{r}_{T,ET}}^{c,k}$ represents the reference state largely unaffected by the fallowed heat island effects of a specific fallowed land, similar to Eqns. 4 and 6 above, where the $\mathrm{T}^{c,k}$ *and* $\mathrm{ET}^{c,k}$ are accessed at the same location of crop type.

In addition, we use ${\hat{r}_{T,ET}}^{c,k}$ to estimate $\hat{\alpha}^{c} = \left(\frac{\partial \hat{\beta}_{T}^{c,k}}{\partial {\hat{r}_{T,ET}}^{c,k}}\right)^{c}$ in Eqn. 10 (see Fig. S25), which is the response of crop yield sensitivity, $\hat{\beta}_{T}^{c,k}$ (Eqn. 9 & Fig. S12), to county-specific crop-specific variabilities in the temperature-moisture coupling, ${\hat{r}_{T,ET}}^{c,k}$ (Fig. S23) using statistical linear regression. That is:

$$\hat{\beta}_{T}^{c,k} = \hat{\alpha}^{c} {\hat{r}_{T,ET}}^{c,k} + \epsilon_{\alpha} \quad (12)$$

Where ϵ_{α} can be associated with the intercept of the regression and other undefined random variables that adds noise to the relationship. Because $\hat{\alpha}^{c}$ represents a change in the standardized coefficient per unit change in correlation between $\mathrm{T}^{c,k}$ and $\mathrm{ET}^{c,k}$, it is dimensionless, which consequently means that $\Delta\beta^{c,k}$ in Eqn. 10 above is also dimensionless.

Therefore, for physical interpretation of the crop yield sensitivity in Eqn. 10 above for locations near the fallowed lands, we convert $\Delta\beta^{c,k}(x,y)$ to a dimensional term by accounting for the county-specific crop-specific variabilities in temperature and crop yield, represented by the standard deviations in nearby surface temperature, $\sigma_{\mathrm{T}}^{c,k}(x,y)$, and crop yield, $\sigma_{\mathrm{Y}}^{c,k}$ (Fig. S26). That is:

$$\Delta B^{c,k}(x,y) = \Delta\beta^{c,k}(x,y) \cdot \frac{\sigma_{Y}^{c,k}}{\sigma_{T}^{c,k}(x,y)} \quad (13)$$

Where $\Delta \mathrm{B}^{c,k}(x,y)$ coefficient having a unit of tons per acre per ^{o}C (Fig. S27 & Fig. 4d). Therefore, to estimate the changes in crop yield that is due to the fallowed heat island effect near the fallowed location, we simply multiply $\Delta \mathrm{B}^{c,k}(x,y)$ with the fallowed heat island

intensity, $\Delta T^{c,k}(x,y)$ (Eqn. 4 & Fig. S28) near the fallowed land for each county and crop type.

$$\Delta Y^{c,k}(x,y) = \Delta B^{c,k}(x,y) \cdot \Delta T^{c,k}(x,y) \quad 14$$

Consequently, we estimate the relative yield impacts ($RYI;\ \%$) on each crop as additional yield loss or gain due to the fallowed heat island effect above the county-wide baseline crop yield. Specifically, we estimate RYI (%) as the percentage of changes in local yields near fallowed land relative to the local baseline yield averaged between 2013 and 2022 ($\frac{1}{N}\sum_t \hat{Y}^{c,k}(t)$; see Fig. S12):

$$RYI\ (\%) = \Delta Y^{c,k}(x,y) \Big/ \frac{1}{N}\sum_t \hat{Y}^{c,k}(t) \quad 15$$

Finally, we average the relative yield impacts (RYI; Fig. S14) across for county, k, in the Central Valley, for crop type, c (corn, cotton, and tomato).

Acknowledgments

We thank Dr. Satyendra Pandey for his thoughtful insight and participation in the discussion during the project meeting session. A.A.A. is supported by grants from the U.S. Department of Energy (DOE) Office of Science (awards #DE-SC0023033) and Hellman Award; M.M.K. by grants from the Climate Action Research Fund from the University of California, Merced, and J.T.A. by grants from the DOE Climate Resilience Center (#DE-SC0024238).

Data Availability

All data used in this study are publicly available. The Cropland Data Layer data can be accessed through the CropScape web application (https://nassgeodata.gmu.edu/CropScape/). Crop yield data were obtained from the USDA National Agricultural Statistics Service (https://quickstats.nass.usda.gov/). Land surface temperature (LST) data were derived from Landsat 8 and accessed via the Google Earth Engine platform (https://earthengine.google.com/). Evapotranspiration (ET) data were obtained from the OpenET project, also available through Google Earth Engine (https://earthengine.google.com/). Processed datasets analyzed in this study to obtain the results are available from the corresponding author upon request, subject to institutional and data use policies.

Code Availability

The codes used in this study to generate the figures are available from the corresponding author upon request, subject to institutional and data use policies.

References

1. T. R. Oke, Towards better scientific communication in urban climate. *Theor. Appl. Climatol.* **84**, 179–190 (2006).

2. J. Jiang, Y. Zhou, X. Guo, T. Qu, Calculation and Expression of the Urban Heat Island Indices Based on GeoSOT Grid. *Sustainability* **14**, 2588 (2022).

3. A. Mohajerani, J. Bakaric, T. Jeffrey-Bailey, The urban heat island effect, its causes, and mitigation, with reference to the thermal properties of asphalt concrete. *J. Environ. Manage.* **197**, 522–538 (2017).

4. L. Yang, F. Qian, D.-X. Song, K.-J. Zheng, Research on Urban Heat-Island Effect. *Procedia Eng.* **169**, 11–18 (2016).

5. F. Mukherjee, D. Singh, Assessing Land Use–Land Cover Change and Its Impact on Land Surface Temperature Using LANDSAT Data: A Comparison of Two Urban Areas in India. *Earth Syst. Environ.* **4**, 385–407 (2020).

6. E. Ng, Policies and technical guidelines for urban planning of high-density cities – air ventilation assessment (AVA) of Hong Kong. *Build. Environ.* **44**, 1478–1488 (2009).

7. G. A. Barron-Gafford, *et al.*, The Photovoltaic Heat Island Effect: Larger solar power plants increase local temperatures. *Sci. Rep.* **6**, 35070 (2016).

8. A. M. Broadbent, E. S. Krayenhoff, M. Georgescu, D. J. Sailor, The Observed Effects of Utility-Scale Photovoltaics on Near-Surface Air Temperature and Energy Balance. *J. Appl. Meteorol. Climatol.* **58**, 989–1006 (2019).

9. V. Fthenakis, Y. Yu, Analysis of the potential for a heat island effect in large solar farms in *2013 IEEE 39th Photovoltaic Specialists Conference (PVSC)*, (IEEE, 2013), pp. 3362–3366.

10. L. Zhao, X. Lee, R. B. Smith, K. Oleson, Strong contributions of local background climate to urban heat islands. *Nature* **511**, 216–219 (2014).

11. K. J. Harding, P. K. Snyder, Modeling the Atmospheric Response to Irrigation in the Great Plains. Part I: General Impacts on Precipitation and the Energy Budget. *J. Hydrometeorol.* **13**, 1667–1686 (2012).

12. D. B. Lobell, C. J. Bonfils, L. M. Kueppers, M. A. Snyder, Irrigation cooling effect on temperature and heat index extremes. *Geophys. Res. Lett.* **35**, 2008GL034145 (2008).

13. N. D. Mueller, *et al.*, Cooling of US Midwest summer temperature extremes from cropland intensification. *Nat. Clim. Change* **6**, 317–322 (2016).

14. Y. Yu, *et al.*, A Numerical Study of the Agricultural Irrigation Effects on Summer Soil Moisture and Near-Surface Meteorology in California's Central Valley. *J. Hydrometeorol.* **26**, 641–659 (2025).

15. F. S. Chapin, P. A. Matson, P. M. Vitousek, *Principles of Terrestrial Ecosystem Ecology* (Springer New York, 2011).

16. H. Taha, Urban climates and heat islands: albedo, evapotranspiration, and anthropogenic heat. *Energy Build.* **25**, 99–103 (1997).

17. A. A. Adebiyi, *et al.*, Fallowed agricultural lands dominate anthropogenic dust sources in California. *Commun. Earth Environ.* **6**, 324 (2025).

18. C. S. A. Wallace, P. Thenkabail, J. R. Rodriguez, M. K. Brown, Fallow-land Algorithm based on Neighborhood and Temporal Anomalies (FANTA) to map planted *versus* fallowed croplands using MODIS data to assist in drought studies leading to water and food security assessments. *GIScience Remote Sens.* **54**, 258–282 (2017).

19. Z. Wu, *et al.*, Seasonal cultivated and fallow cropland mapping using MODIS-based automated cropland classification algorithm. *J. Appl. Remote Sens.* **8**, 083685 (2014).

20. Y. Xie, *et al.*, Cropland abandonment between 1986 and 2018 across the United States: spatiotemporal patterns and current land uses. *Environ. Res. Lett.* **19**, 044009 (2024).

21. E. S. K. Vick, P. C. Stoy, A. C. I. Tang, T. Gerken, The surface-atmosphere exchange of carbon dioxide, water, and sensible heat across a dryland wheat-fallow rotation. *Agric. Ecosyst. Environ.* **232**, 129–140 (2016).

22. T. R. Oke, The energetic basis of the urban heat island. *Q. J. R. Meteorol. Soc.* **108**, 1–24 (1982).

23. J. Henao, C. Baanante, “Estimating Rates of Nutrient Depletion in Soils of Agricultural Lands of Africa” in (International Fertilizer Development Center (IFDC), 1999), p. 87.

24. E. Hanak, *et al.*, Water and the Future of the San Joaquin Valley. (2019). https://doi.org/10.13140/RG.2.2.24360.83208.

25. S. Dharumarajan, *et al.*, Biophysical and socio-economic causes for increasing fallow land in Tamil Nadu. *Soil Use Manag.* **33**, 487–498 (2017).

26. V. Espinoza, *et al.*, From fallow ground to common ground: Perspectives on future land uses in the San Joaquin valley under sustainable groundwater management. *J. Environ. Manage.* **333**, 117226 (2023).

27. O. Mertz, C. Mbow, A. Reenberg, A. Diouf, Farmers’ Perceptions of Climate Change and Agricultural Adaptation Strategies in Rural Sahel. *Environ. Manage.* **43**, 804–816 (2009).

28. F. Alonso-Sarría, C. Martínez-Hernández, A. Romero-Díaz, F. Cánovas-García, F. Gomariz-Castillo, Main Environmental Features Leading to Recent Land Abandonment in Murcia Region (Southeast Spain). *Land Degrad. Dev.* **27**, 654–670 (2016).

29. D. C. Nielsen, F. J. Calderón, “Fallow Effects on Soil” in *Soil Management: Building a Stable Base for Agriculture*, J. L. Hatfield, T. J. Sauer, Eds. (Soil Science Society of America, 2015), pp. 287–300.

30. T. Nelson, *et al.*, Economic and Water Supply Effects of Ending Groundwater Overdraft in California's Central Valley. *San Franc. Estuary Watershed Sci.* **14** (2016).

31. E. Hanak, *et al.*, Water stress and a changing San Joaquin Valley. (2017). https://doi.org/10.13140/RG.2.2.31739.31522.

32. S. Siebert, F. Ewert, E. Eyshi Rezaei, H. Kage, R. Graß, Impact of heat stress on crop yield—on the importance of considering canopy temperature. *Environ. Res. Lett.* **9**, 044012 (2014).

33. S. C. Zipper, *et al.*, Urban heat island impacts on plant phenology: intra-urban variability and response to land cover. *Environ. Res. Lett.* **11**, 054023 (2016).

34. J. L. Hatfield, J. H. Prueger, Temperature extremes: Effect on plant growth and development. *Weather Clim. Extrem.* **10**, 4–10 (2015).

35. C. Zhao, *et al.*, Temperature increase reduces global yields of major crops in four independent estimates. *Proc. Natl. Acad. Sci.* **114**, 9326–9331 (2017).

36. D. B. Lobell, K. N. Cahill, C. B. Field, Historical effects of temperature and precipitation on California crop yields. *Clim. Change* **81**, 187–203 (2007).

37. D. B. Lobell, W. Schlenker, J. Costa-Roberts, Climate Trends and Global Crop Production Since 1980. *Science* **333**, 616–620 (2011).

38. D. B. Lobell, C. B. Field, Global scale climate–crop yield relationships and the impacts of recent warming. *Environ. Res. Lett.* **2**, 014002 (2007).

39. J. L. Hatfield, J. H. Prueger, Temperature extremes: Effect on plant growth and development. *Weather Clim. Extrem.* **10**, 4–10 (2015).

40. California's Central Valley | USGS California Water Science Center. Available at: https://ca.water.usgs.gov/projects/central-valley/about-central-valley.html [Accessed 22 August 2025].

41. C. Boryan, Z. Yang, R. Mueller, M. Craig, Monitoring US agriculture: the US Department of Agriculture, National Agricultural Statistics Service, Cropland Data Layer Program. *Geocarto Int.* **26**, 341–358 (2011).

42. K. Sayler, "Landsat 8-9 Collection 2 (C2) Level 2 Science Product (L2SP) Guide" (USGS, 2023).

43. K. Tan, Z. Liao, P. Du, L. Wu, Land surface temperature retrieval from Landsat 8 data and validation with geosensor network. *Front. Earth Sci.* **11**, 20–34 (2017).

44. J. M. Volk, *et al.*, Assessing the accuracy of OpenET satellite-based evapotranspiration data to support water resource and land management applications. *Nat. Water* **2**, 193–205 (2024).

45. D. Zhou, S. Zhao, L. Zhang, G. Sun, Y. Liu, The footprint of urban heat island effect in China. *Sci. Rep.* **5**, 11160 (2015).

46. K. Knipper, *et al.*, A comparative analysis of OpenET for evaluating evapotranspiration in California almond orchards. *Agric. For. Meteorol.* **355**, 110146 (2024).

47. C. Lesk, *et al.*, Compound heat and moisture extreme impacts on global crop yields under climate change. *Nat. Rev. Earth Environ.* **3**, 872–889 (2022).

48. C. Lesk, *et al.*, Stronger temperature–moisture couplings exacerbate the impact of climate warming on global crop yields. *Nat. Food* **2**, 683–691 (2021).

49. I. Becker-Reshef, E. Vermote, M. Lindeman, C. Justice, A generalized regression-based model for forecasting winter wheat yields in Kansas and Ukraine using MODIS data. *Remote Sens. Environ.* **114**, 1312–1323 (2010).

50. J. Ren, Z. Chen, Q. Zhou, H. Tang, Regional yield estimation for winter wheat with MODIS-NDVI data in Shandong, China. *Int. J. Appl. Earth Obs. Geoinformation* **10**, 403–413 (2008).

51. Q. Yang, X. Huang, Q. Tang, Irrigation cooling effect on land surface temperature across China based on satellite observations. *Sci. Total Environ.* **705**, 135984 (2020).

52. V. Mishra, *et al.*, Moist heat stress extremes in India enhanced by irrigation. *Nat. Geosci.* **13**, 722–728 (2020).

53. J. O. Payero, D. D. Tarkalson, S. Irmak, D. Davison, J. L. Petersen, Effect of irrigation amounts applied with subsurface drip irrigation on corn evapotranspiration, yield, water use efficiency, and dry matter production in a semiarid climate. *Agric. Water Manag.* **95**, 895–908 (2008).

54. L. Shashua-Bar, M. E. Hoffman, Vegetation as a climatic component in the design of an urban street. *Energy Build.* **31**, 221–235 (2000).

55. R. A. Spronken-Smith, T. R. Oke, W. P. Lowry, Advection and the surface energy balance across an irrigated urban park. *Int. J. Climatol.* **20**, 1033–1047 (2000).

56. D. Zhou, S. Zhao, L. Zhang, G. Sun, Y. Liu, The footprint of urban heat island effect in China. *Sci. Rep.* **5**, 11160 (2015).

57. K. Furtak, A. Wolińska, The impact of extreme weather events as a consequence of climate change on the soil moisture and on the quality of the soil environment and agriculture – A review. *CATENA* **231**, 107378 (2023).

58. A. García-García, *et al.*, Soil heat extremes can outpace air temperature extremes. *Nat. Clim. Change* **13**, 1237–1241 (2023).

59. K. J. McFarlane, *et al.*, Experimental warming and drying increase older carbon contributions to soil respiration in lowland tropical forests. *Nat. Commun.* **15**, 7084 (2024).

60. L. H. Baumgard, *et al.*, “Impact of Climate Change on Livestock Production” in *Environmental Stress and Amelioration in Livestock Production*, V. Sejian, S. M. K. Naqvi, T. Ezeji, J. Lakritz, R. Lal, Eds. (Springer Berlin Heidelberg, 2012), pp. 413–468.

61. S. P. Parajuli, *et al.*, Impact of irrigation on farmworkers’ heat stress in California differs by season and during the day and night. *Commun. Earth Environ.* **5**, 787 (2024).

62. M. Segal, R. W. Arritt, Nonclassical Mesoscale Circulations Caused by Surface Sensible Heat-Flux Gradients. *Bull. Am. Meteorol. Soc.* **73**, 1593–1604 (1992).

63. T. Chakraborty, X. Lee, Land Cover Regulates the Spatial Variability of Temperature Response to the Direct Radiative Effect of Aerosols. *Geophys. Res. Lett.* **46**, 8995–9003 (2019).

64. C. E. Bulgin, *et al.*, Quantifying Uncertainty in Satellite-Retrieved Land Surface Temperature from Cloud Detection Errors. *Remote Sens.* **10**, 616 (2018).

65. D. Ghent, *et al.*, A New Approach to Defining Uncertainties for MODIS Land Surface Temperature. *Remote Sens.* **11**, 1021 (2019).

66. B. N. Tran, *et al.*, Uncertainty assessment of satellite remote-sensing-based evapotranspiration estimates: a systematic review of methods and gaps. *Hydrol. Earth Syst. Sci.* **27**, 4505–4528 (2023).

67. K. Sayler, Landsat 8-9 Collection 2 (C2) Level 2 Science Product (L2SP) Guide. Deposited May 2024.

68. A. J. Oliphant, *et al.*, Automated Cropland Fallow Algorithm (ACFA) for the Northern Great Plains of USA. *Int. J. Digit. Earth* **17**, 2337221 (2024).

69. Z. Yang, *et al.*, Impact of Irrigation over the California Central Valley on Regional Climate. *J. Hydrometeorol.* **18**, 1341–1357 (2017).

70. T. J. Lark, I. H. Schelly, H. K. Gibbs, Accuracy, Bias, and Improvements in Mapping Crops and Cropland across the United States Using the USDA Cropland Data Layer. *Remote Sens.* **13**, 968 (2021).

71. T. J. Lark, R. M. Mueller, D. M. Johnson, H. K. Gibbs, Measuring land-use and land-cover change using the U.S. department of agriculture’s cropland data layer: Cautions and recommendations. *Int. J. Appl. Earth Obs. Geoinformation* **62**, 224–235 (2017).

72. V. Ihlen, *Landsat 8 (L8) Data Users Handbook* (USGS, 2019).

73. Earth Resources Observation and Science (EROS) Center, Landsat 8-9 Operational Land Imager / Thermal Infrared Sensor Level-1, Collection 2. U.S. Geological Survey. https://doi.org/10.5066/P975CC9B. Deposited 2013.

74. Landsat 8 | U.S. Geological Survey. (2023). Available at: https://www.usgs.gov/landsat-missions/landsat-8 [Accessed 22 August 2025].

75. G. Mancino, A. Ferrara, A. Padula, A. Nolè, Cross-Comparison between Landsat 8 (OLI) and Landsat 7 (ETM+) Derived Vegetation Indices in a Mediterranean Environment. *Remote Sens.* **12**, 291 (2020).

76. D. P. Roy, *et al.*, Characterization of Landsat-7 to Landsat-8 reflective wavelength and normalized difference vegetation index continuity. *Remote Sens. Environ.* **185**, 57–70 (2016).

77. Earth Resources Observation and Science (EROS) Center, Landsat 8-9 Operational Land Imager / Thermal Infrared Sensor Level-2, Collection 2. U.S. Geological Survey. https://doi.org/10.5066/P9OGBGM6. Deposited 2013.

78. N. Gorelick, *et al.*, Google Earth Engine: Planetary-scale geospatial analysis for everyone. *Remote Sens. Environ.* **202**, 18–27 (2017).

79. B. Pu, P. Ginoux, Projection of American dustiness in the late 21st century due to climate change. *Sci. Rep.* **7**, 5553 (2017).

80. U. Avdan, G. Jovanovska, Algorithm for Automated Mapping of Land Surface Temperature Using LANDSAT 8 Satellite Data. *J. Sens.* **2016**, 1–8 (2016).

81. H. An, H. Cai, X. Xu, Z. Qiao, D. Han, Impacts of Urban Green Space on Land Surface Temperature from Urban Block Perspectives. *Remote Sens.* **14**, 4580 (2022).

82. G. Faqe Ibrahim, Urban Land Use Land Cover Changes and Their Effect on Land Surface Temperature: Case Study Using Dohuk City in the Kurdistan Region of Iraq. *Climate* **5**, 13 (2017).

83. Q. Weng, D. Lu, J. Schubring, Estimation of land surface temperature–vegetation abundance relationship for urban heat island studies. *Remote Sens. Environ.* **89**, 467–483 (2004).

84. J. A. Sobrino, J. C. Jiménez-Muñoz, L. Paolini, Land surface temperature retrieval from LANDSAT TM 5. *Remote Sens. Environ.* **90**, 434–440 (2004).

85. T. N. Carlson, D. A. Ripley, On the relation between NDVI, fractional vegetation cover, and leaf area index. *Remote Sens. Environ.* **62**, 241–252 (1997).

86. Y. Cui, X. Xu, J. Dong, Y. Qin, Influence of Urbanization Factors on Surface Urban Heat Island Intensity: A Comparison of Countries at Different Developmental Phases. *Sustainability* **8**, 706 (2016).

87. R. Emmanuel, E. Krüger, Urban heat island and its impact on climate change resilience in a shrinking city: The case of Glasgow, UK. *Build. Environ.* **53**, 137–149 (2012).

88. E. J. Good, An in situ-based analysis of the relationship between land surface "skin" and screen-level air temperatures. *J. Geophys. Res. Atmospheres* **121**, 8801–8819 (2016).

89. Z. Li, *et al.*, Satellite Remote Sensing of Global Land Surface Temperature: Definition, Methods, Products, and Applications. *Rev. Geophys.* **61**, e2022RG000777 (2023).

90. X. Lian, *et al.*, Spatiotemporal variations in the difference between satellite-observed daily maximum land surface temperature and station-based daily maximum near-surface air temperature. *J. Geophys. Res. Atmospheres* **122**, 2254–2268 (2017).

91. M. Anderson, *et al.*, Field-Scale Assessment of Land and Water Use Change over the California Delta Using Remote Sensing. *Remote Sens.* **10**, 889 (2018).

92. K. Knipper, *et al.*, A comparative analysis of OpenET for evaluating evapotranspiration in California almond orchards. *Agric. For. Meteorol.* **355**, 110146 (2024).

93. F. S. Melton, *et al.*, OpenET: Filling a Critical Data Gap in Water Management for the Western United States. *JAWRA J. Am. Water Resour. Assoc.* **58**, 971–994 (2022).

94. Z. Sun, Q. Wang, O. Batkhishig, Z. Ouyang, Relationship between Evapotranspiration and Land Surface Temperature under Energy- and Water-Limited Conditions in Dry and Cold Climates. *Adv. Meteorol.* **2016**, 1–9 (2016).

95. M. Adil, *et al.*, Effects of Fallow Management Practices on Soil Water, Crop Yield and Water Use Efficiency in Winter Wheat Monoculture System: A Meta-Analysis. *Front. Plant Sci.* **13**, 825309 (2022).

96. C. Brouwer, M. Heibloem, "Irrigation Water Management: Irrigation Water Needs" (Food and Agriculture Organization of the United Nations, 1986).

97. P. Döll, Impact of Climate Change and Variability on Irrigation Requirements: A Global Perspective. *Clim. Change* **54**, 269–293 (2002).

98. Y. Guo, Y. Shen, Agricultural water supply/demand changes under projected future climate change in the arid region of northwestern China. *J. Hydrol.* **540**, 257–273 (2016).

99. M. Irizarry-Ortiz, E. W. Harmsen, Sensitivity of the Penman–Monteith Reference Evapotranspiration Equation to Meteorological Variables for Puerto Rico. *Hydrology* **10**, 101 (2023).

100. D. B. Lobell, C. B. Field, Global scale climate–crop yield relationships and the impacts of recent warming. *Environ. Res. Lett.* **2**, 014002 (2007).

101. C. Zhao, *et al.*, Temperature increase reduces global yields of major crops in four independent estimates. *Proc. Natl. Acad. Sci.* **114**, 9326–9331 (2017).

102. F. A. Vogel, G. A. Bange, "Understanding USDA Crop Forecasts" (National Agricultural Statistics Service and Office of the Chief Economist, World Agricultural Outlook Boar, 1999).

103. E. K. Carter, J. Melkonian, S. J. Riha, S. B. Shaw, Separating heat stress from moisture stress: analyzing yield response to high temperature in irrigated maize. *Environ. Res. Lett.* **11**, 094012 (2016).

104. A. J. Rigden, N. D. Mueller, N. M. Holbrook, N. Pillai, P. Huybers, Combined influence of soil moisture and atmospheric evaporative demand is important for accurately predicting US maize yields. *Nat. Food* **1**, 127–133 (2020).

105. S. Siebert, H. Webber, G. Zhao, F. Ewert, Heat stress is overestimated in climate impact studies for irrigated agriculture. *Environ. Res. Lett.* **12**, 054023 (2017).

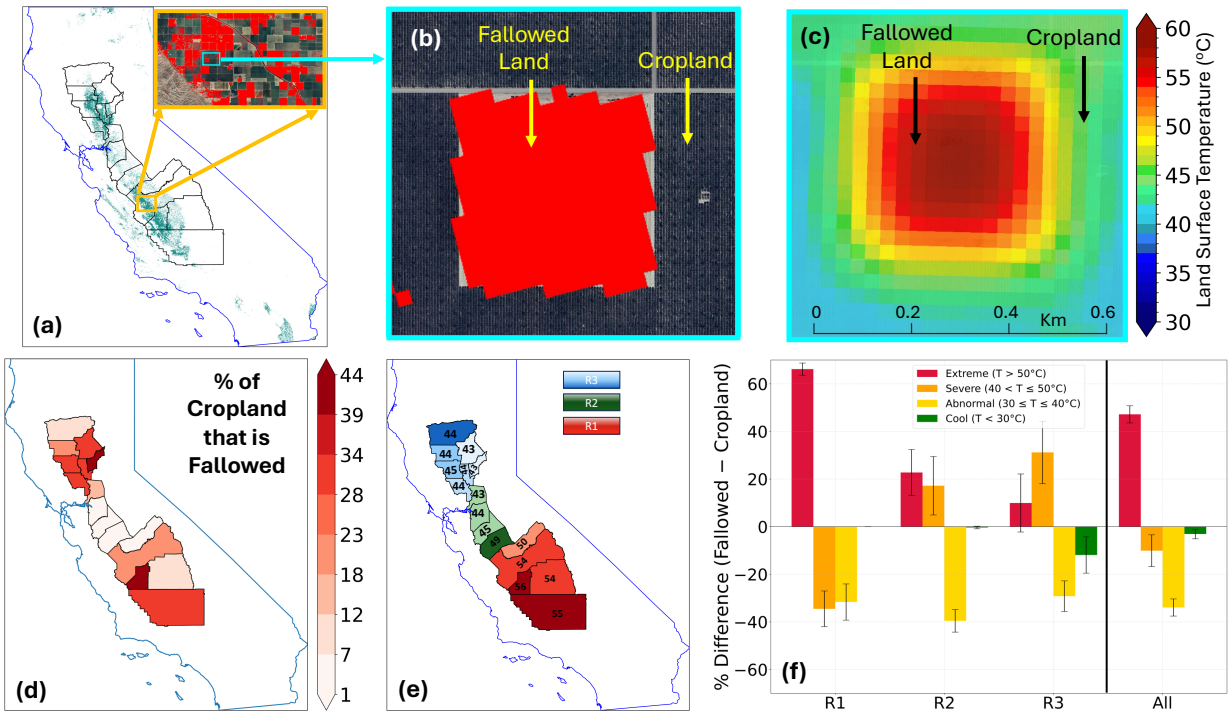

Fig. 1: Isolated fallowed lands often have higher surface temperature than surrounding croplands. The figure shows (a) all the density of fallowed locations between 2013 and 2022; The inserted yellow box in shows a close-up satellite image of fallowed (red) and cultivated (green) croplands from Fresno County in 2015; (b) Cluster of fallowed fields (red) surrounded by active croplands (dark green), with (c) the surface temperature (T)

signature obtained from the Landsat8 and averaged over June–August 2015; (d) percent of croplands that is fallowed in Central Valley County between 2013 and 2022; (e) County-level surface temperature over fallowed locations across three subregions (southern part the San Joaquin Valley, R1, the northern part of San Joaquin Valley and Metro Sacramento, R2, and the northern part of Sacramento Valley, R3); (f) percentage differences between fallowed land and active croplands or agricultural land coverages with extreme ($T > 50^oC$), severe ($40^oC < T \leq 50^oC$), abnormal ($30^oC \leq T \leq 40^oC$) and cool ($T < 30^oC$) surface temperatures; Positive values denotes fallowed lands accounts for more of the temperature category than croplands, and vice versa for negative values. Black lines on bars in (c) are the standard deviations.

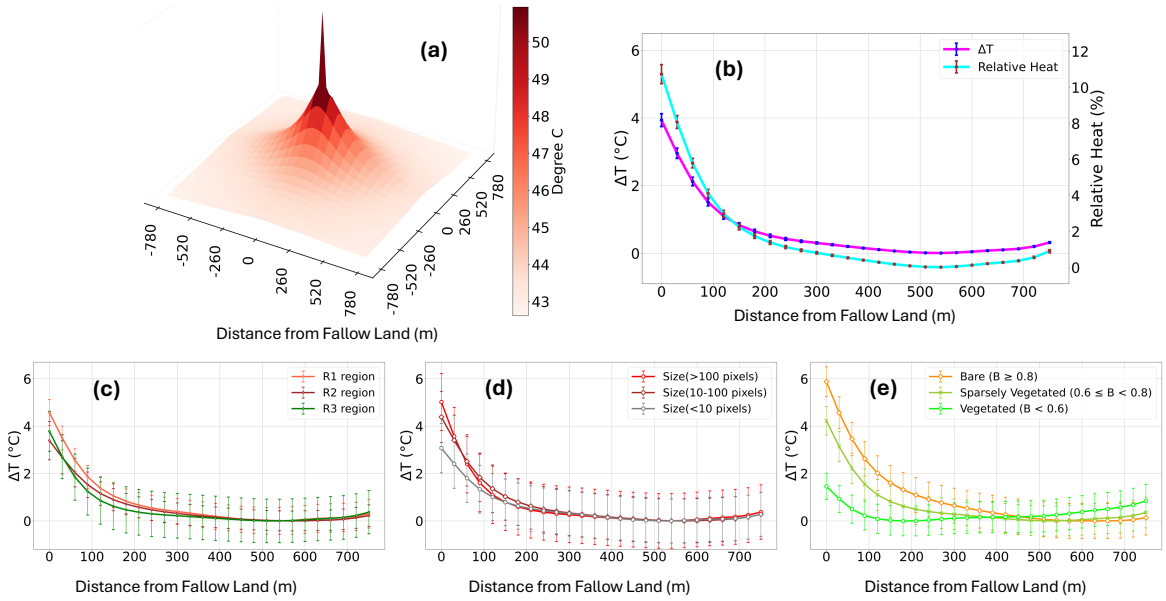

Fig. 2: Fallowed Heat Island Effect across California's Central Valley. (a) The surface temperature (T, °C) of cropland region surrounding a centered fallowed lands averaged between 2013 and 2022; (b) Fallowed heat island intensity (ΔT, °C; magenta line) and relative heat (%; cyan line) averaged across all directions of croplands surrounding fallowed lands; The Fallowed heat island intensity (ΔT, °C) (c) divided into subregions within Central Valley (R1 (green), R2 (brown), and R3 (orange); (see Fig. 1e for definition), (d) as a function of fallowed land size/coverage defined by the number of 900-m^2 pixels for < 10 pixels (gray), 10-100 pixels (brown), and >100 pixels (light red); and (e) as a function of surface bareness ($B < 0.6$ (light green), $0.6 \leq B < 0.8$ (green), $B \geq 0.8$ (orange)). Vertical lines in panels (b–e) are standard errors and denote variability in the estimates across counties.

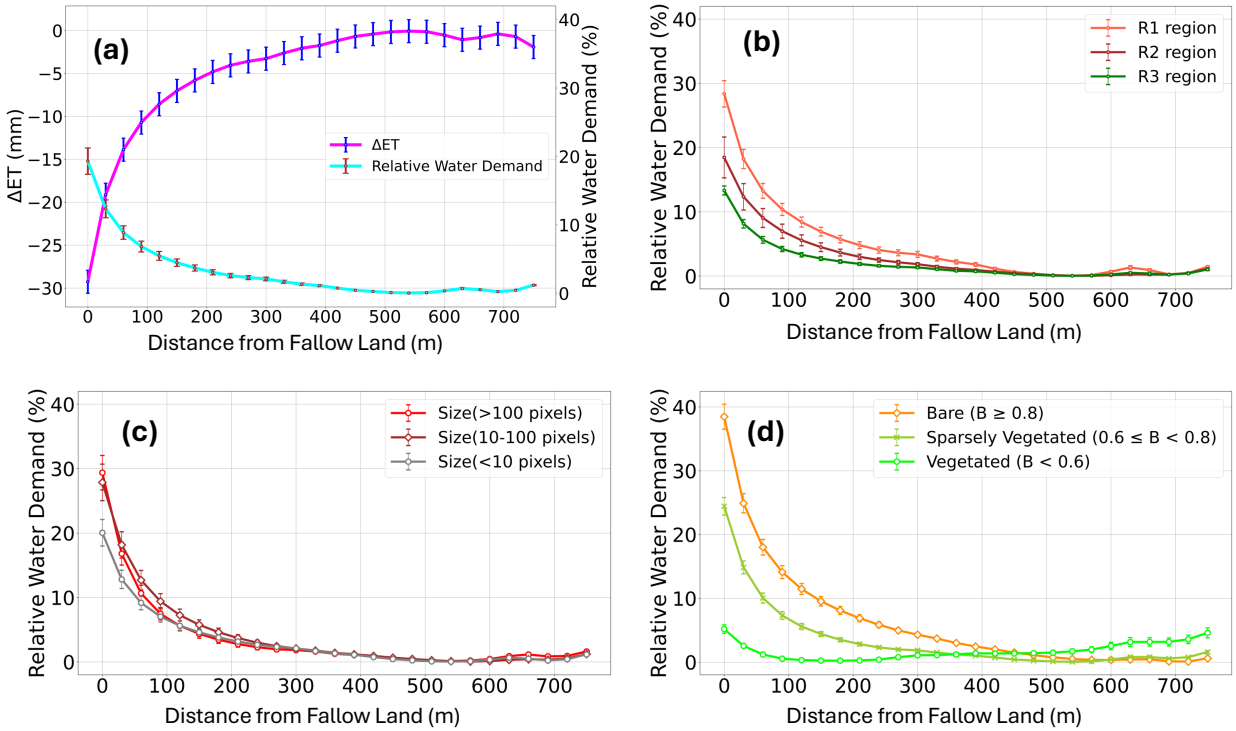

Fig. 3: Effects of Fallowed Heat Island on evapotranspiration and relative water demand. (a) The effects of the fallowed heat island on evapotranspiration (ΔET, mm; magenta) and relative water demand (%; cyan line) of croplands surrounding fallowed lands across the Central Valley; (b) Relative water demand of croplands surrounding fallowed lands across three subregions (R1–R3; see Fig. 1e for definition); (c) as a function of fallowed land size/coverage defined by the number of 900-m^2 pixels for < 10 pixels (gray), 10-100 pixels (brown), and >100 pixels (light red); and (d) as a function of surface bareness (B < 0.6 (light green), 0.6 ≤ B < 0.8 (green), B ≥ 0.8 (orange)). Vertical lines in panels (a–d) are standard errors and denote variability in the estimates across counties.

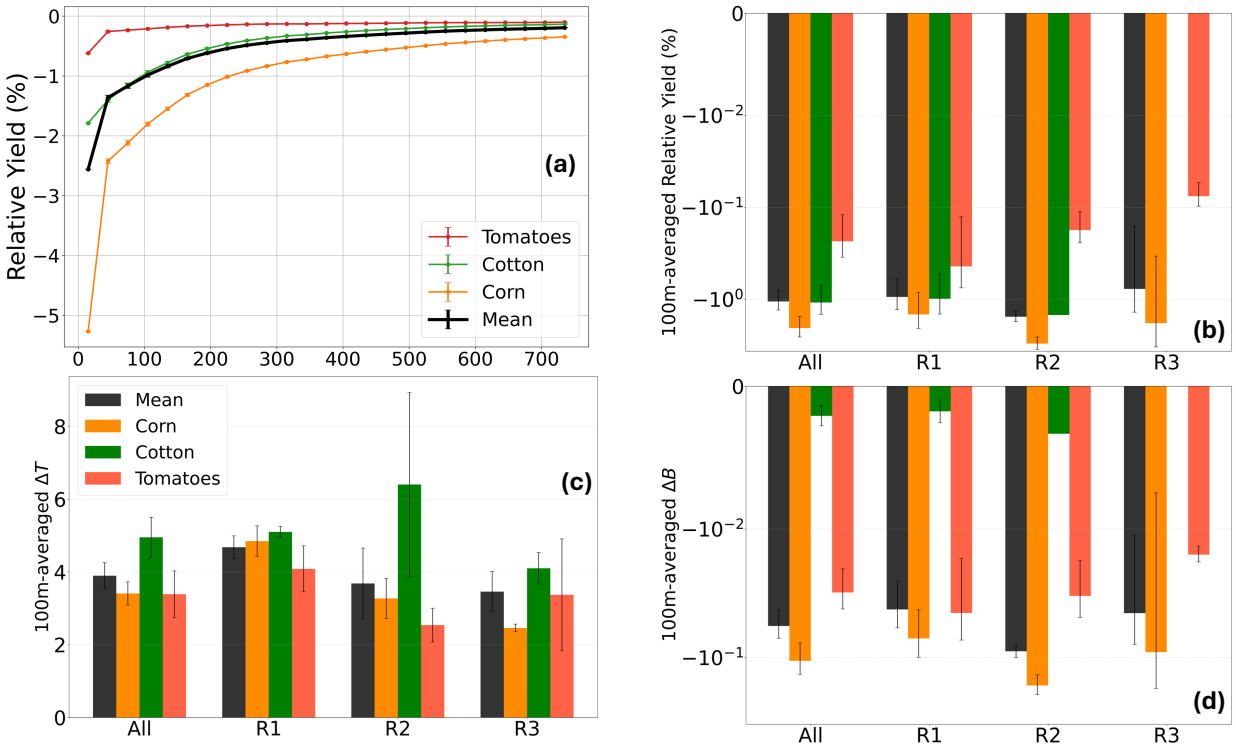

Fig. 4: Effects of Fallowed Heat Island on crop productivity. (a) The relative yield response (%) due to fallowed heat island for corn (orange), cotton (green), and tomatoes (light red), with the three-crop mean response (black); Comparison of (b) relative yield impacts (%), (c) fallowed heat island intensity (ΔT ºC), and (d) response of crop yield sensitivity to variabilities in the temperature-moisture coupling for Tomatoes (red bars), Cotton (green bars) and Corn (orange bars), and all three crops (black bars) averaged for the 100-m near the fallowed lands across all counties (All) and each subregions (R1, R2 and R3). Standard error bars in (a) denote variability in the estimates across counties, and in (b–d) across grid cells.

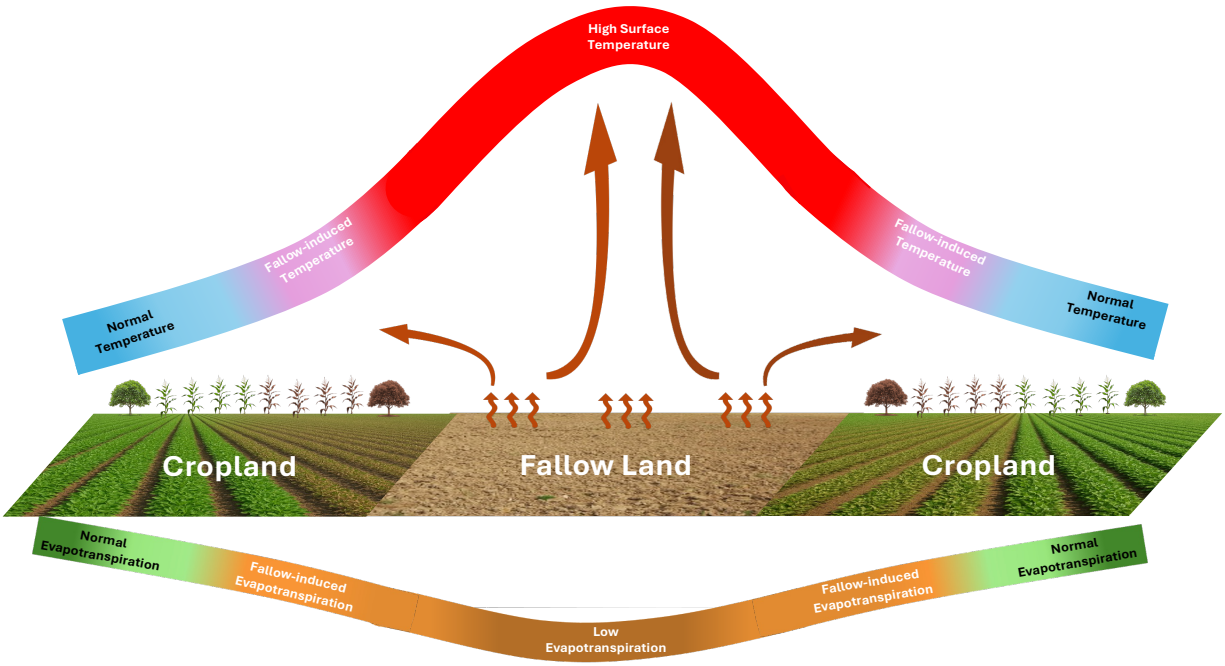

Fig. 5: Fallowed Heat Island Effect. Elevated heat generated from the fallow lands spread to the adjacent croplands, increasing surface temperature, evapotranspiration deficit, and irrigated water demand, ultimately leading to a reduction in crop yield and productivity.

Supplementary Information for

Fallowed Heat Island: High surface temperature from fallowed agricultural lands increases nearby water demand and reduces crop yield.

Md. Minhazul Kibria[1], Adeyemi A. Adebiyi[1], John T. Abatzoglou[2]

[1]*Department of Life and Environmental Sciences, University of California, Merced*

[2]*Department of Management of Complex Systems, University of California, Merced.*

*Corresponding author: Adeyemi A. Adebiyi

Email: aaadebiyi@ucmerced.edu

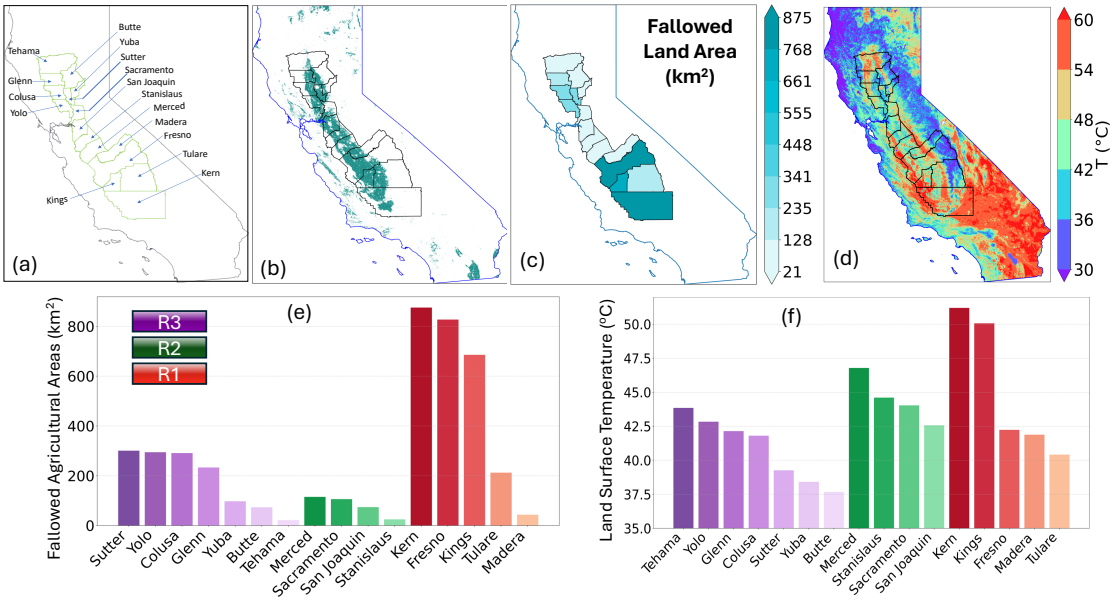

Fig. S1: **Total fallowed land area (km²) and its surface temperature (°C) in the Central Valley.** (a) All counties in the Central Valley; (b) All cropland locations from 2013 to 2022 across California; (c) Total fallowed land (area in km²) averaged over the period 2013-2022 for each county in the Central Valley; (d) Distribution of June-August (2013-2022) mean surface temperature (T, °C) across California; (e) Total fallowed land area of each county across three region in the Central Valley and (f) Surface temperature of the fallowed locations across three regions where the shades of color indicate three study regions: R1 (red bars), R2 (dark green bars), and R3 (purple bars) in the Central Valley (see Fig. 1e).

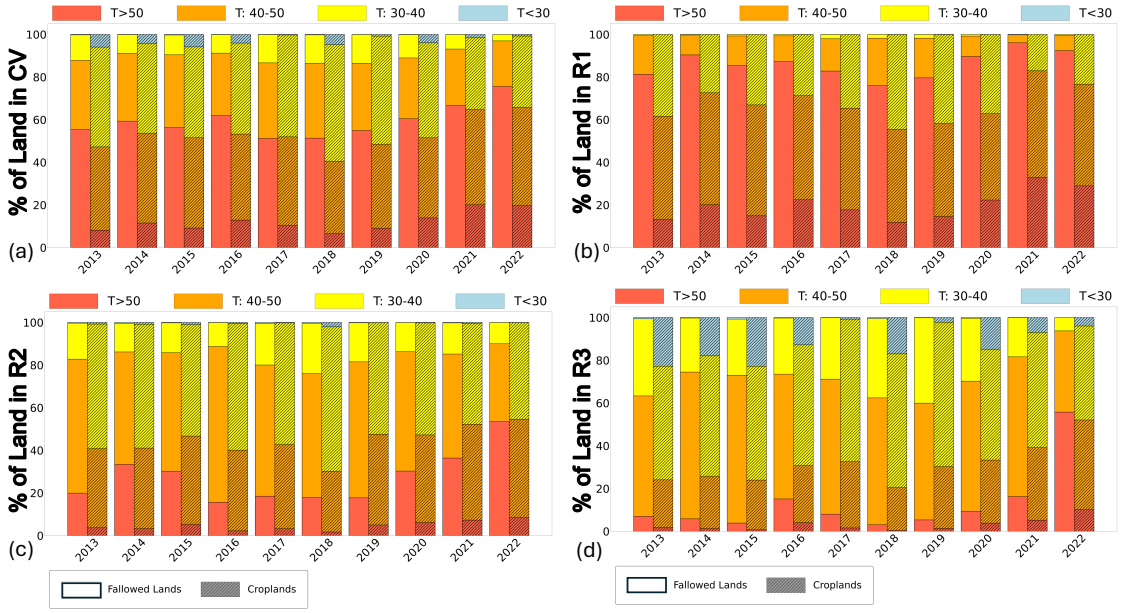

Fig. S2: **Surface characteristics of fallowed lands.** *(a) The percentage contributions of extreme T>50 °C (light red bars), abnormal T between 40-50 °C (orange bars), normal T between 30-40 °C (yellow bars), and cool T<30 °C (light blue bars) conditions, defined respectively as 12-month averaged T over the fallowed locations (solid bars) and agricultural locations (dashed bars) in Central Valley; (b) in R1 region; (c) R2 region; and (d) R3 region.*

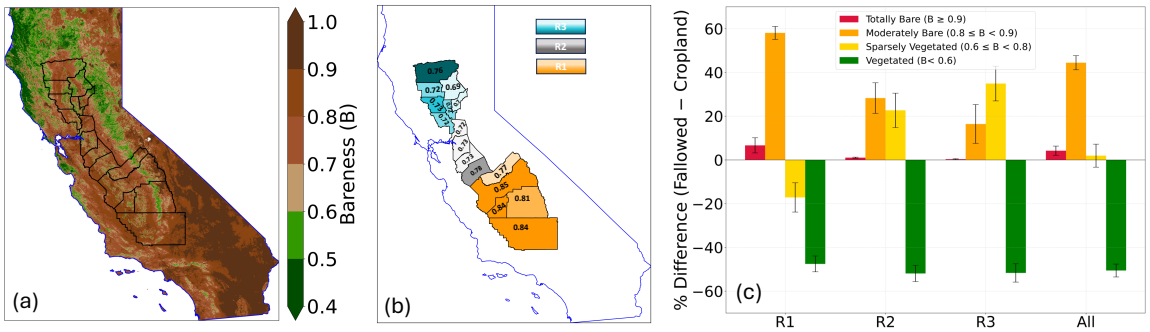

Fig. S3: **Surface condition of fallowed land.** (a) Distribution of June-August (2013-2022) mean surface bareness across California; See Methods for definition of surface bareness; (b) county-scale bareness over fallowed lands across subregions; (c) percentage differences in bare surface categories between fallowed and active croplands. Black lines on bars in Fig. (c) are the standard deviations.

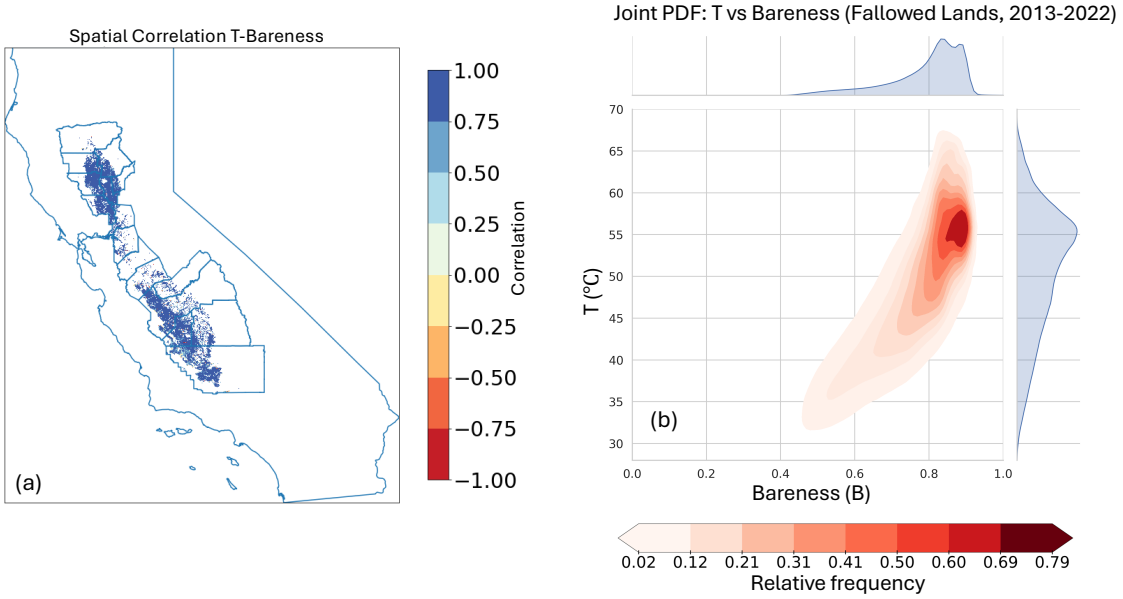

Fig. S4**: Fallowed lands show higher bareness and surface temperature in the Central Valley of California.** (a) Correlation between surface temperature (T, °C) and Bareness in the Central Valley. (b) Probability density function (pdf) of the temperature (T, °C) and Bareness jointly showing that the higher number of fallowed lands corresponds to the higher temperature (T > 50°C, y-axis) and higher bareness (B > 0.78, x-axis), indicating pdf values greater than 0.50.

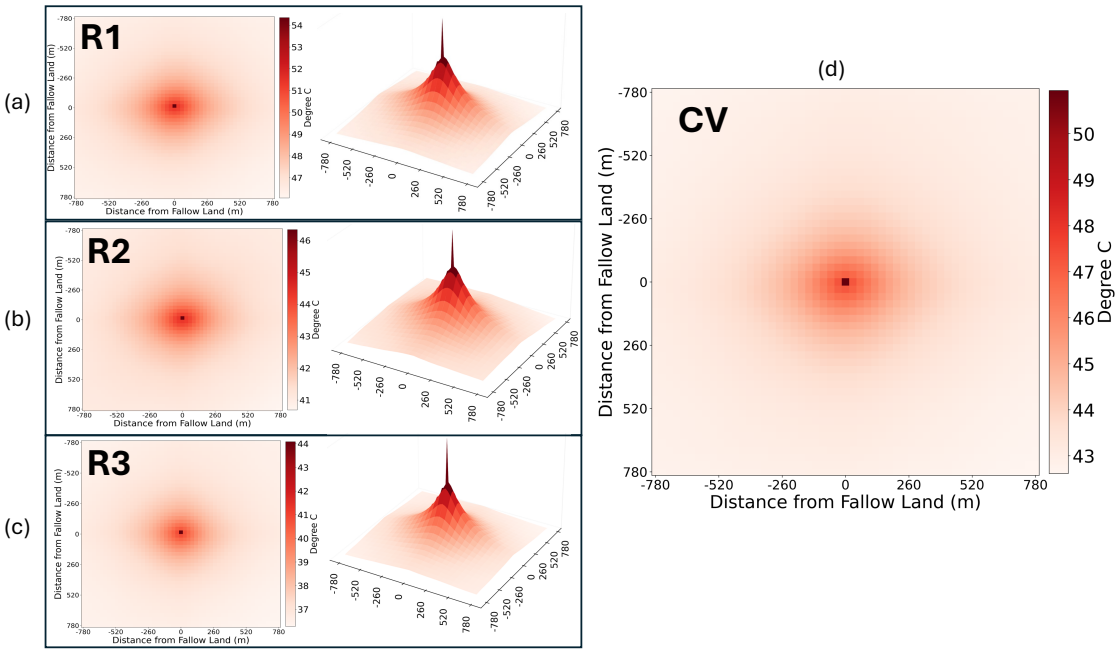

Fig. S5: **Fallowed lands show higher surface temperature compared to the surrounding agricultural croplands.** The surface temperature (T, °C) of the cropland region (780 × 780 m²) surrounding a centered fallowed land averaged between 2013 and 2022, shown in a 2-D image and 3-D for (a) R1, (b), and (c) R3 regions (see Fig. 2e for definition), and (d) Central Valley (CV).

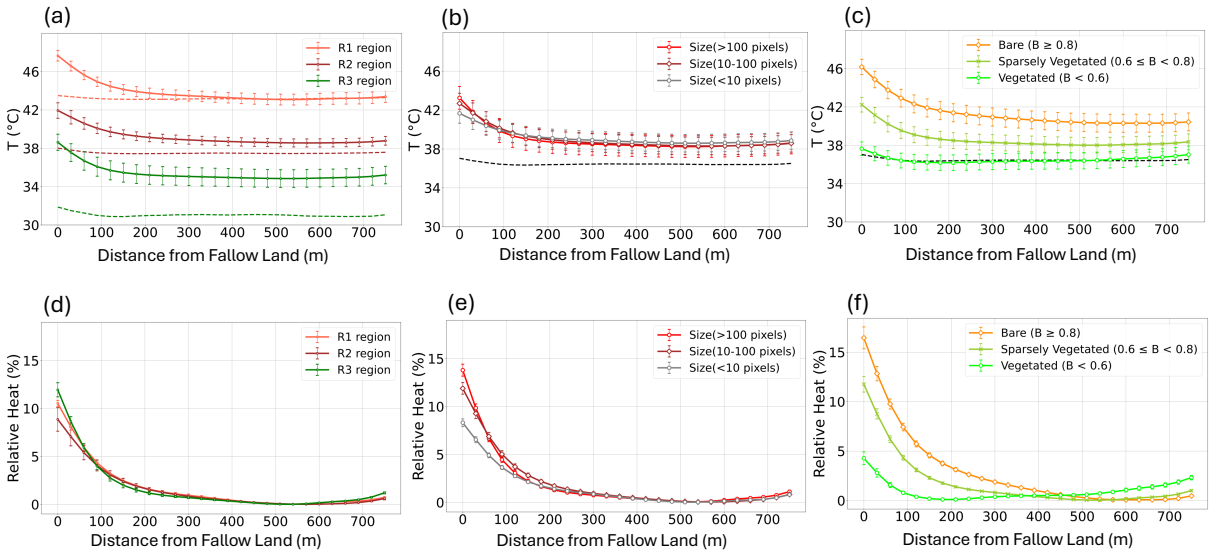

Fig. S6: **Fallowed Heat Island effect also depends on regions, sizes of fallowed lands, and bareness of the fallowed lands.** Same as Fig. 2c, 2d, and 2e, but for mean surface temperature T (°C) and relative heat (%) as a function of different regions, fallow land sizes, and bareness values. Error bars represent standard error.

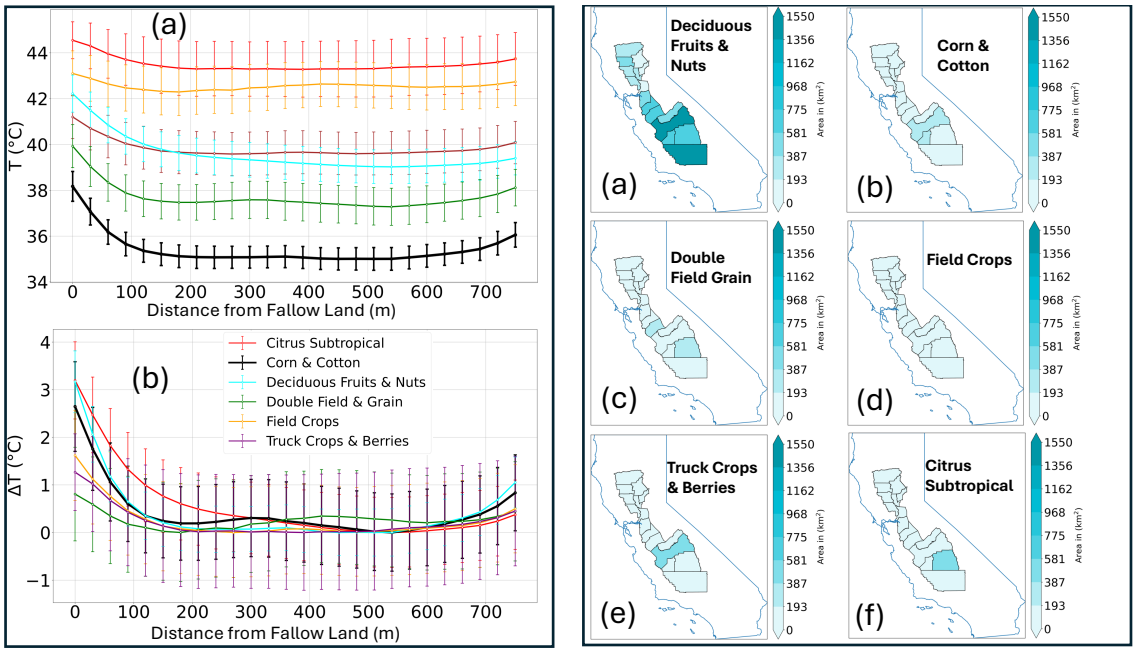

92

93 Fig. S7: **Fallowed Heat Island effect on different crop categories.** Same as Fig. 2c, d, e, but for
94 different crops. Right column: (a) Mean temperature and (b) Difference between mean and
95 reference temperature. Error bars represent standard error. Left column: Same as Fig. S1c but for
96 different crop categories.

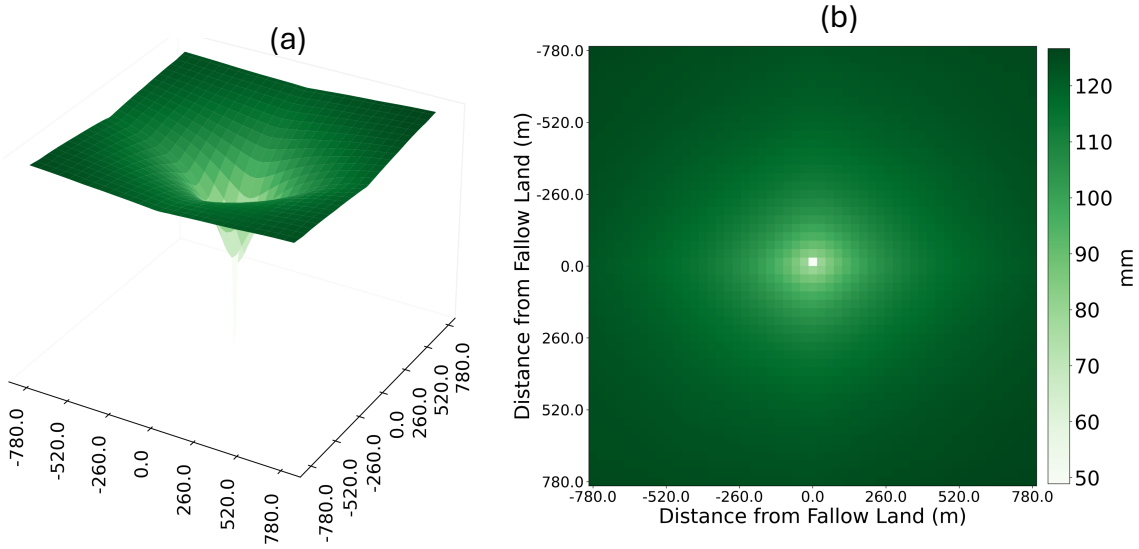

97 Fig. S8: **Fallowed lands exhibit lower ET compared to the surrounding agricultural lands.** Same
98 as Fig. 2a and Fig. S5d but for ET.

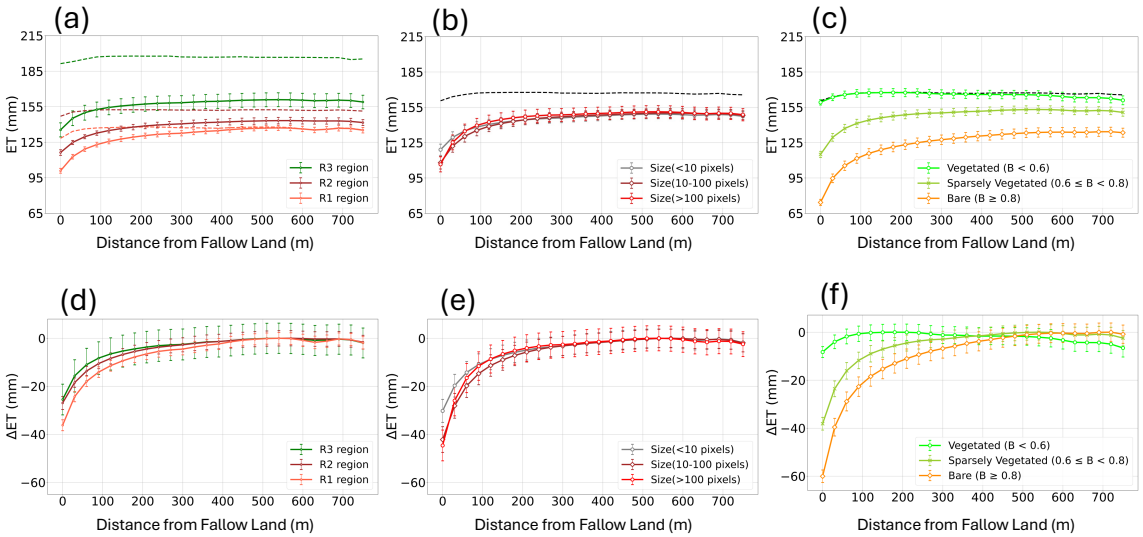

99 Fig. S9: **Fallowed lands effects on evapotranspiration of the surrounding agricultural croplands.**
100 Same as Fig. S6 but for ET.

101

102

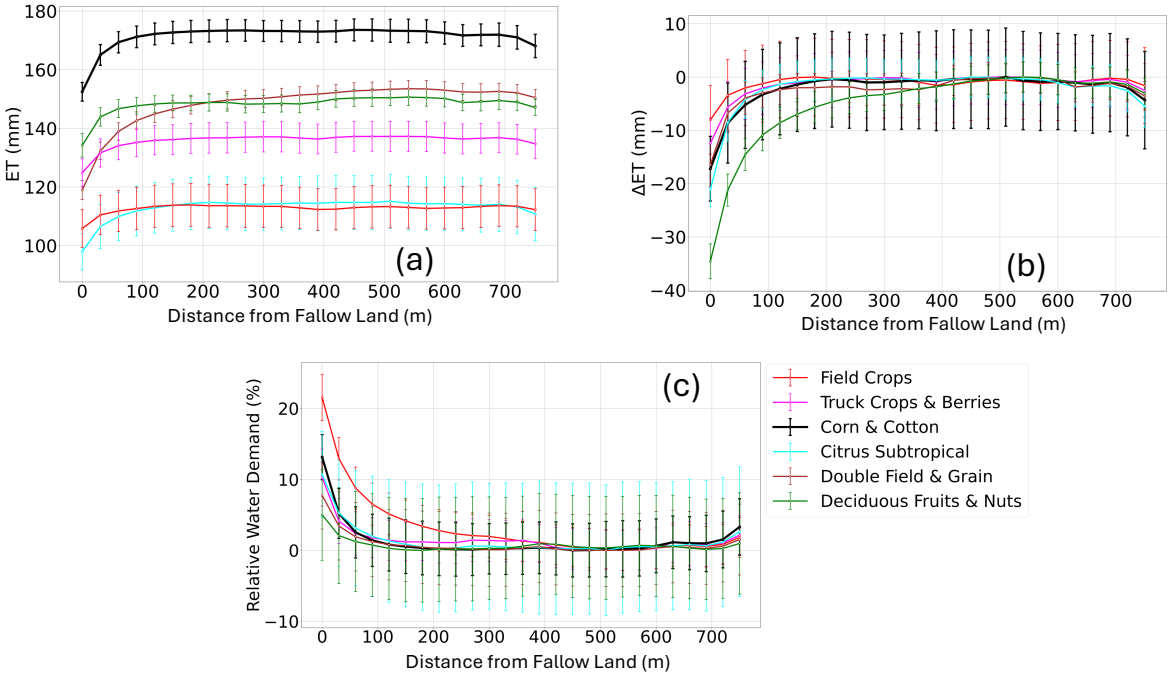

103 Fig. S10: **Impact of fallowed land-generated heat island effect on the water demand of different**
104 **crop categories.** Same as Fig. S7 but for ET.

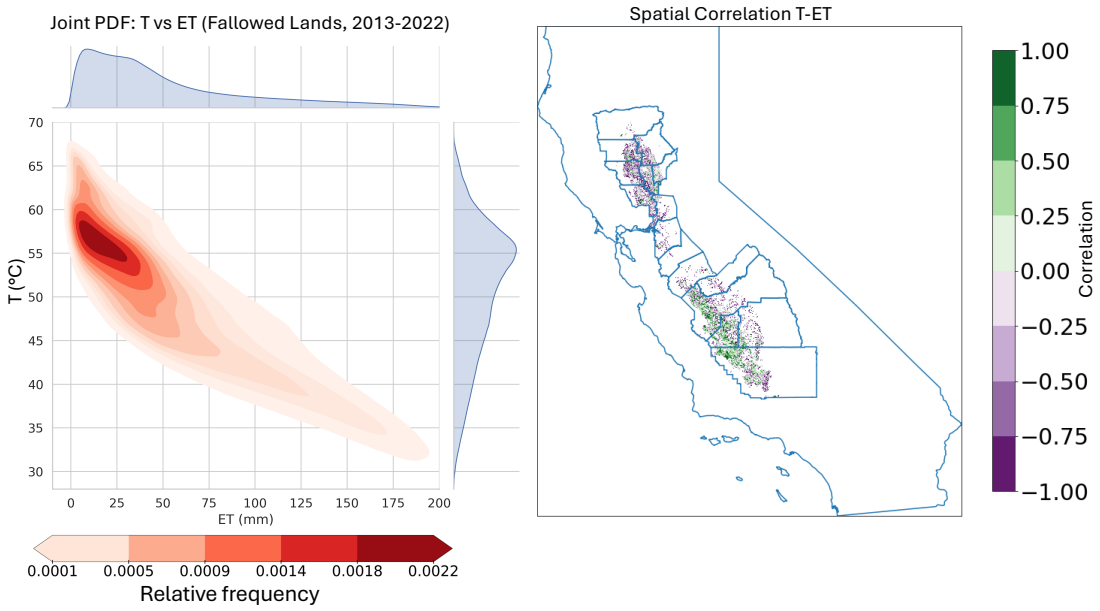

105 Fig. S11: **Fallowed locations show higher surface temperature (T, °C) and lower ET in the Central**
106 **Valley of California.** Same as Fig. S4 but for ET.

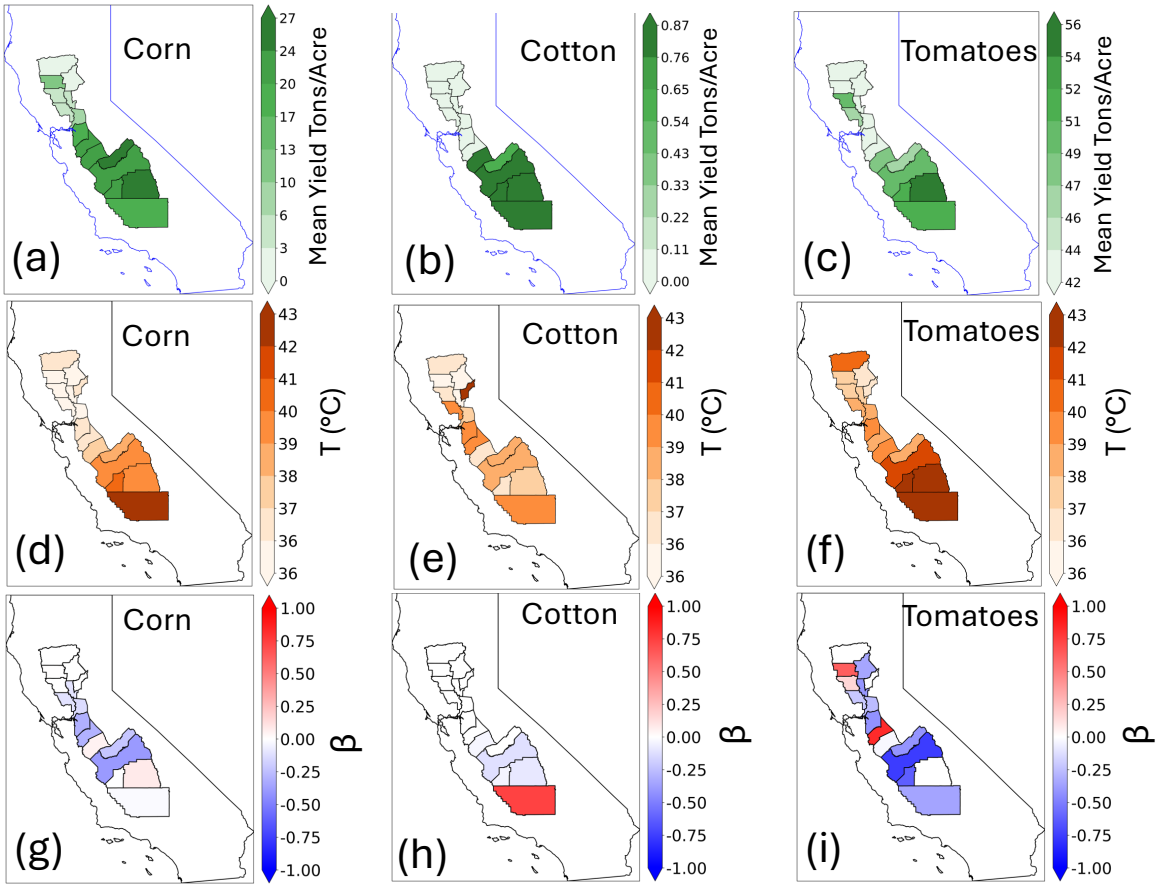

Fig. S12: **County-wise variability in mean crop yield, temperature, and crop yield response (beta) for Corn, Cotton, and Tomatoes.** Mean crop yield in Tons/Acre for (a) Corn, (b) Cotton, and (c) Tomatoes. (d), (e) and (f) show the temperature of these crop locations averaged over the period 2013-2022. (g), (h) and (i) show the regression slope between crop yield and temperature, β for these crops (See Eqn. 9 in Method).

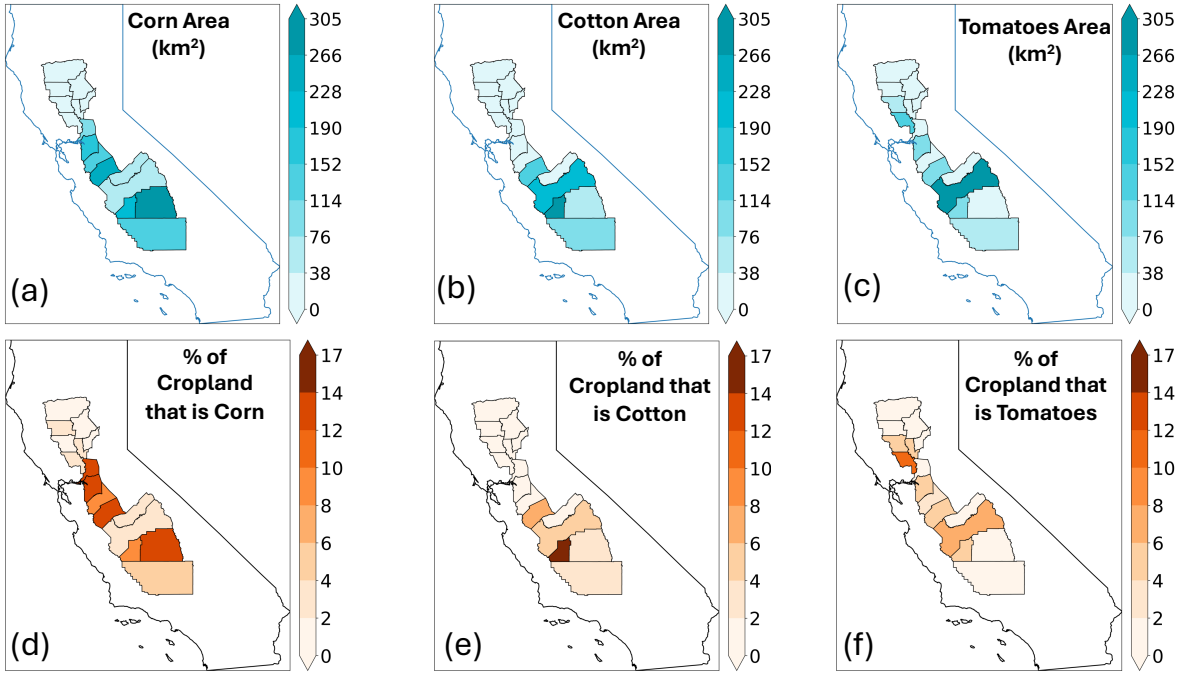

Fig. S13: **Spatial variability of total area and percentage land occupied by Corn, Cotton, and Tomatoes in the Central Valley**. Same as Fig. 1d and Fig. S1c but for Corn, Cotton, and Tomatoes.

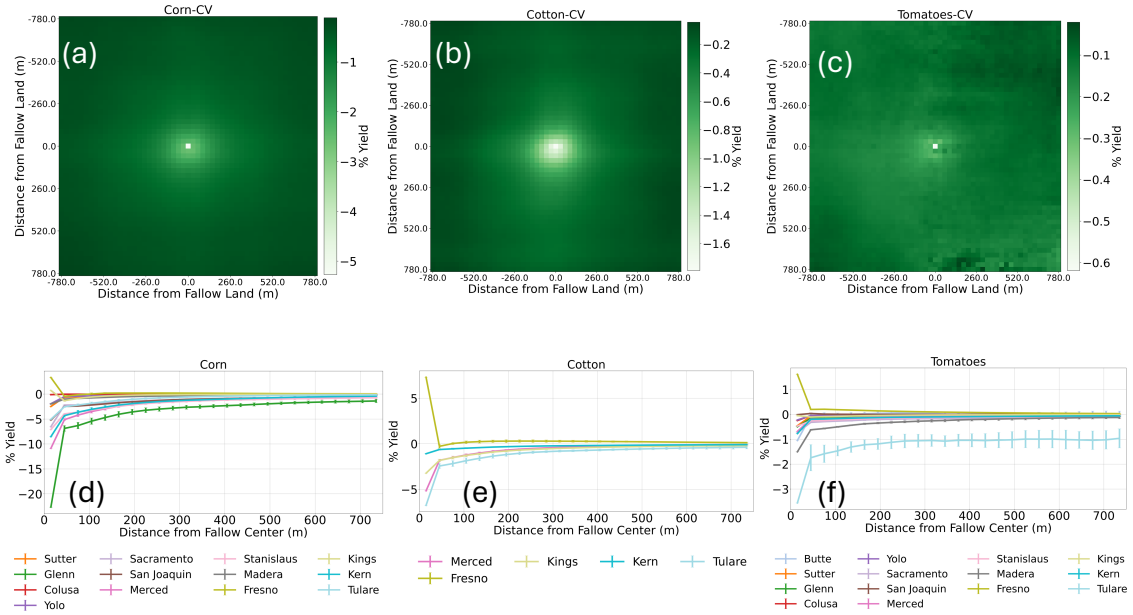

116

117 Fig. S14: **Percentage of yield for different crops in individual counties in the Central Valley**. Same
118 as Fig. S5 but for different crops and yield percentage (a) Corn, (b) Cotton, and (c) Tomatoes. Lines
119 in (d), (e), and (f) show the % yield for each country.

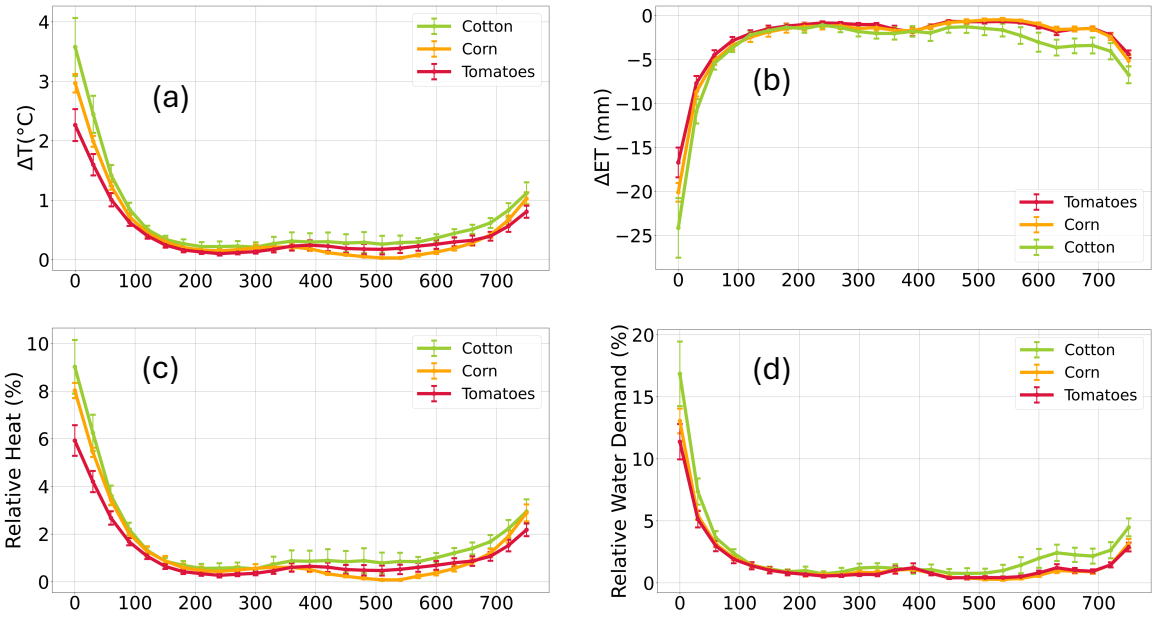

120

121 Fig. S15: **Fallowed heat island effect on Corn, Cotton, and Tomatoes.** (a), (c) same as Fig. 2c but
122 for different crops. (b) and (d) same as Fig. 3a but for different crops.

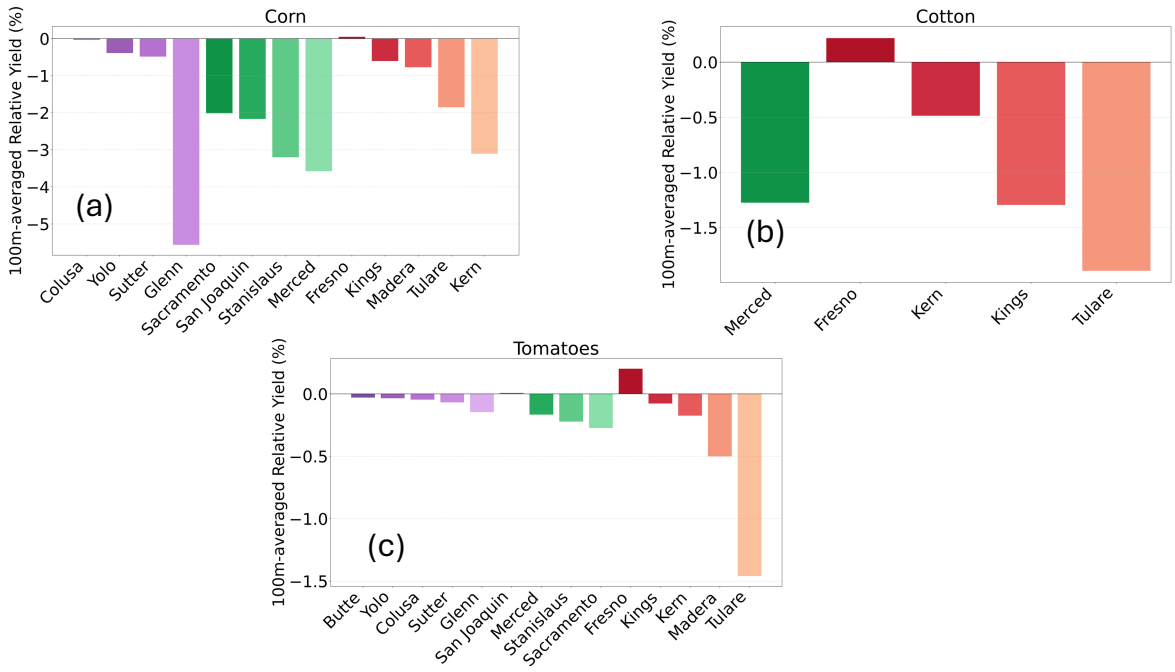

123

124 Fig. S16: **Relative yield in percentage for Corn, Cotton, and Tomatoes averaged over the first 100**
125 **m from the fallowed center.** Same as Fig. 4b but for different crops.

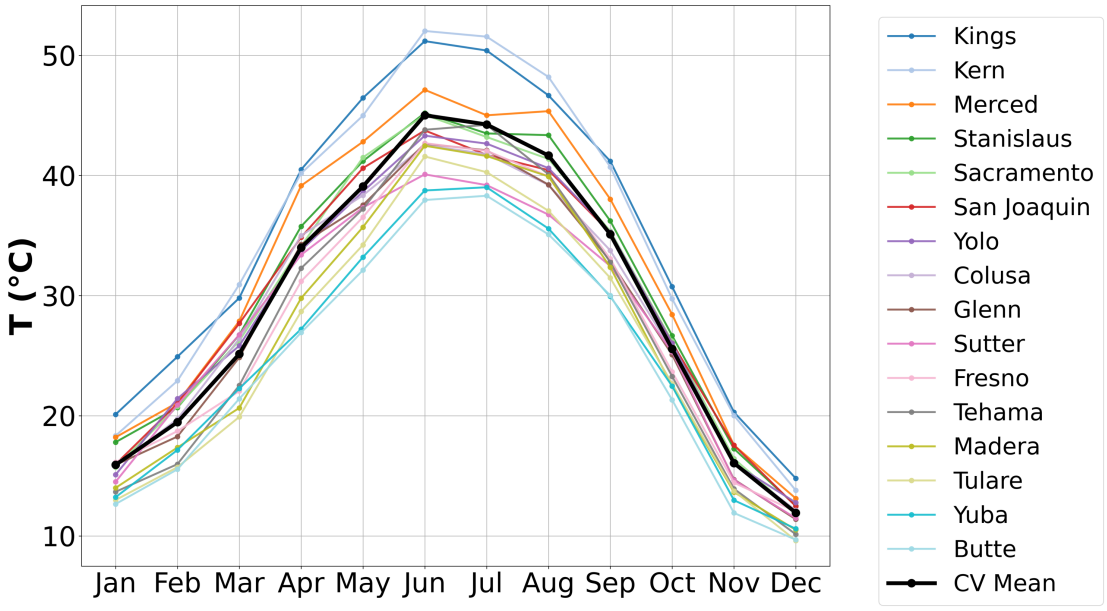

126 Fig. S17: **All counties in the Central Valley have higher land surface temperature (T, °C) during**
127 **the summer months (JJA).** Monthly climatology of the surface temperature (T, °C) in California's
128 Central Valley averaged between 2013 and 2022.

129

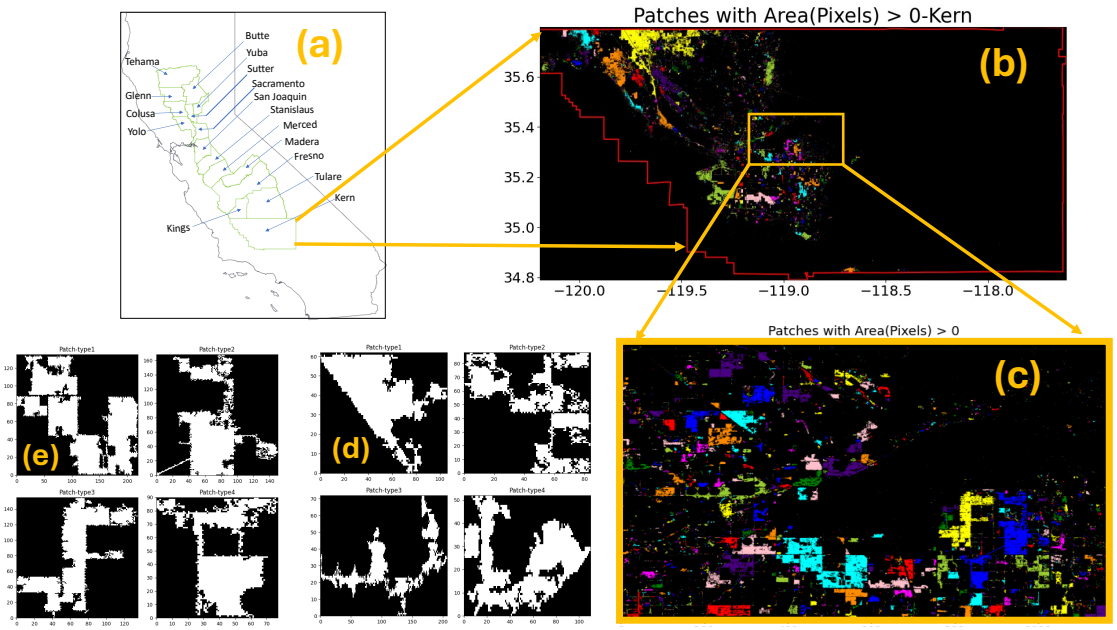

Fig. S18: **Different sizes and shapes of fallowed lands in the Central Valley**. (a) Geographical locations of California's Central Valley. (b) All Fallowed lands (isolated and part of a larger cluster) in Kern County, as an example. The yellow box in (c) shows the approximate region in (b). (d) and (e) The Top eight fallowed the cluster's shape from (c).

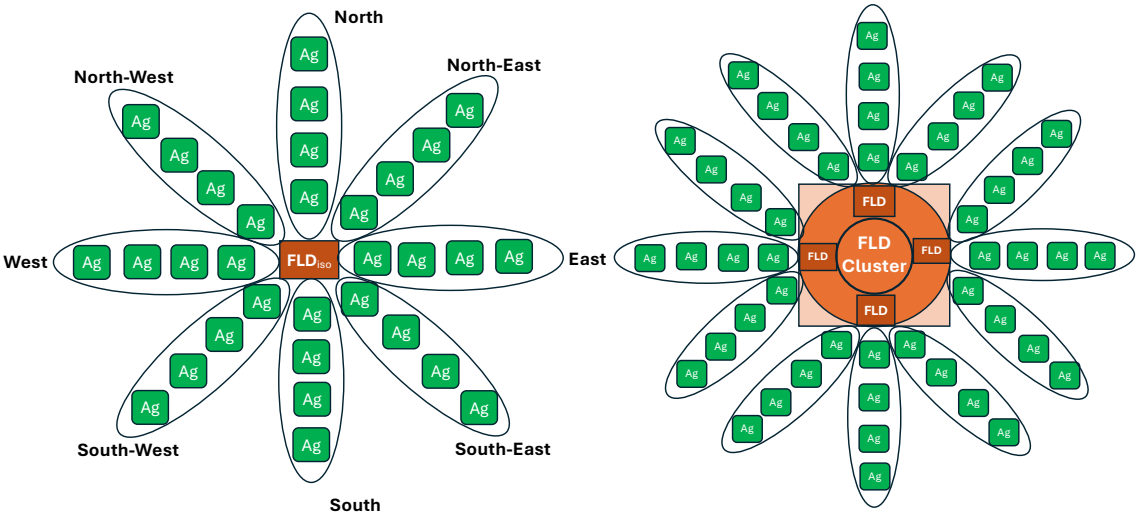

Fig. S19: **Schematic diagram showing how consecutive agricultural lands surrounding the (a) isolated fallowed land and (b) fallowed land being part of a larger cluster were taken in the analysis.**

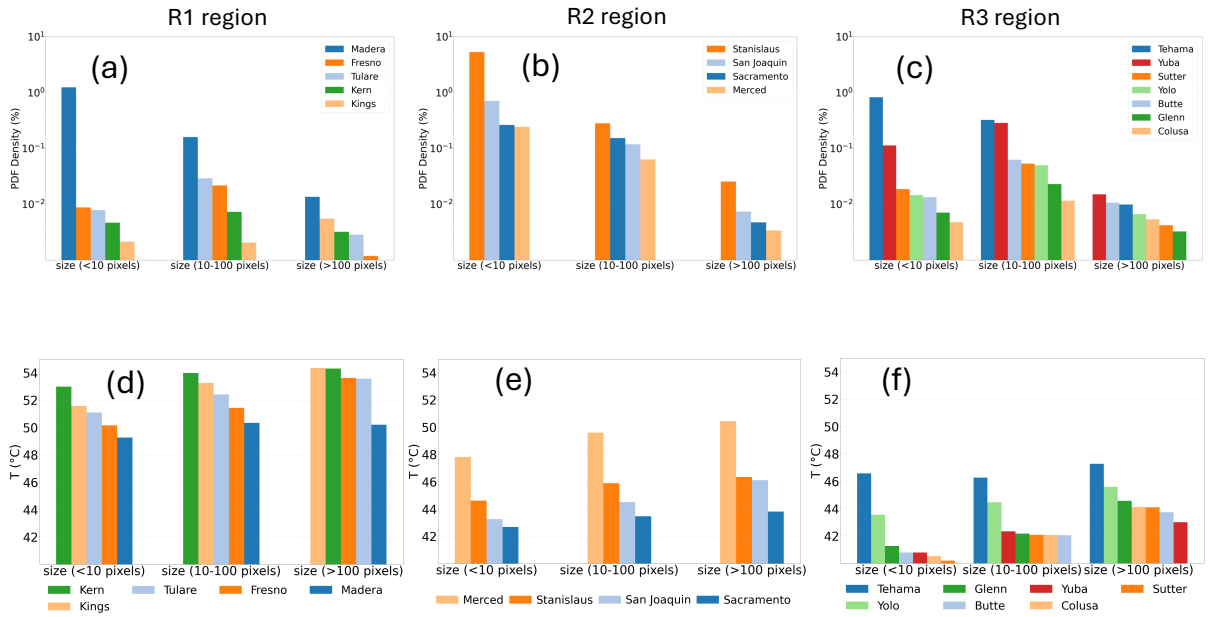

Fig. S20: **Larger fallowed lands have higher surface temperature, while they are lower in numbers**. PDF of the number of pixels in a fallowed land patch (cluster of fallow land) as a function of counties in R1 (a), R2 (b), and R3 (c), and fallowed land sizes (see the three columns in the x-axis). Mean surface temperature (T, °C) vs different fallowed land sizes (total number of connected pixels) as a function of counties (d), (e), and (f) corresponds to R1, R2, and R3 regions, respectively.

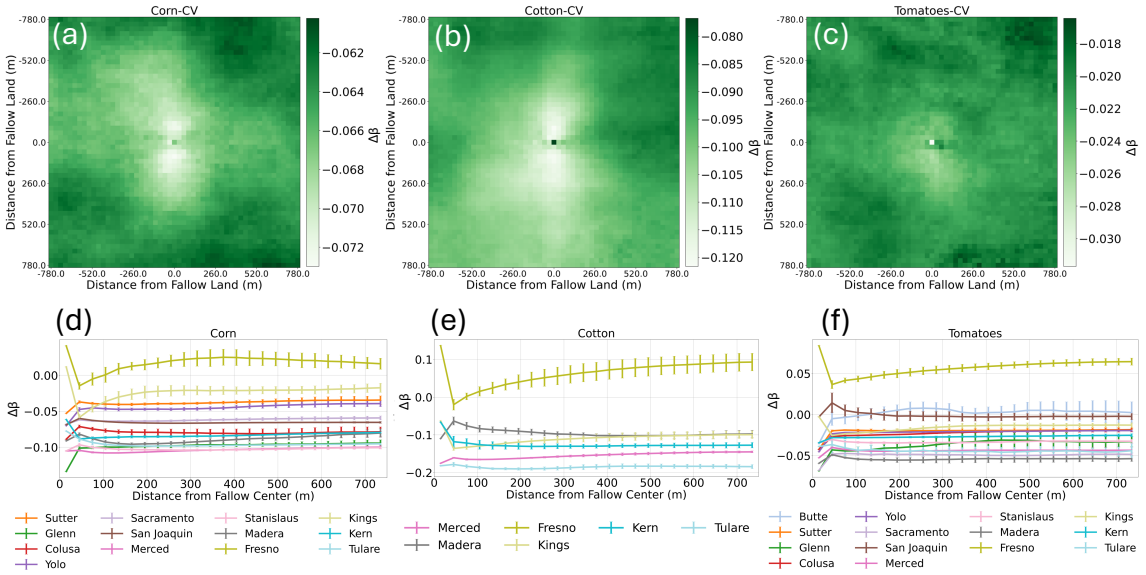

150 Fig. S21: **Crop yield sensitivity (Δβ) varies for different counties in the Central Valley**. (a), (b), and
151 (c) same as Fig. S5 but for Δ β (see Methods) and different crops. Lines in (d), (e), and (f) show the
152 Δ β for each country.

153

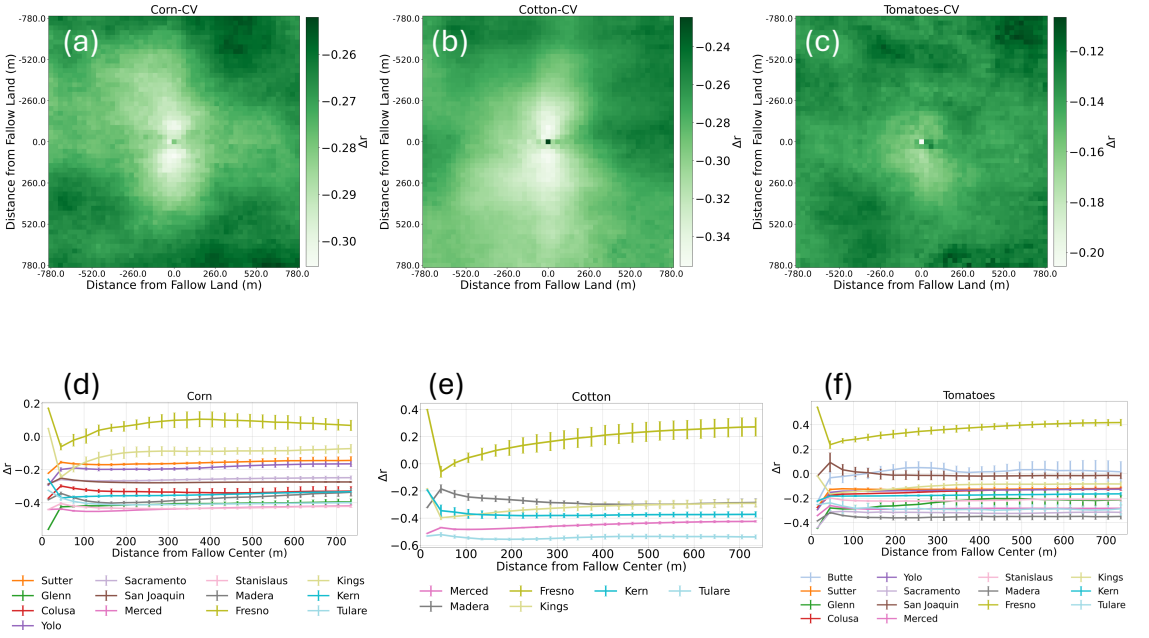

154

155 Fig. S22: **County-level changes (Δr) in the correlation between temperature (T, °C) and**
156 **evapotranspiration (ET) across the Central Valley.** Same as Fig. S21 but for Δr.

157

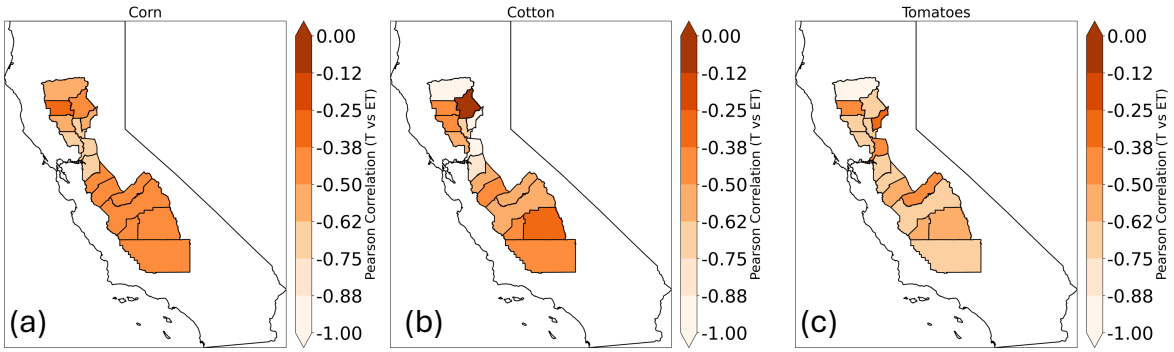

Fig. S23: **Spatial variability in Pearson correlation for each county and each crop**. Pearson correlation between T and ET for (a) Corn, (b) Cotton, and (c) Tomatoes.

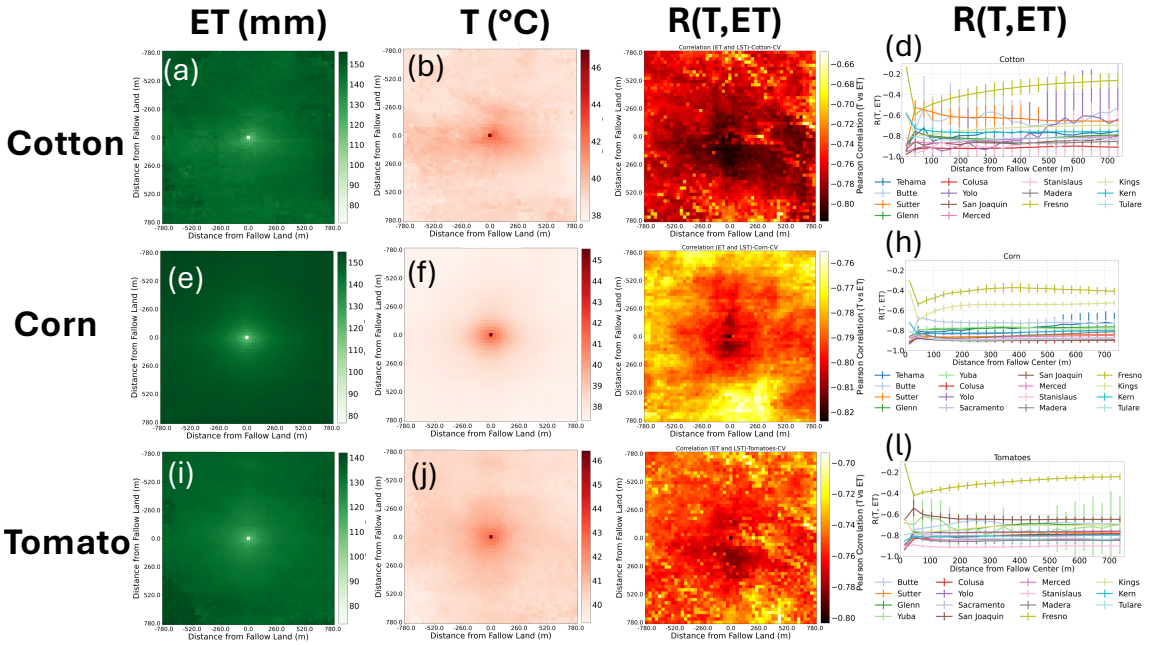

Fig. S24: **Fallowed lands disrupt crop water–temperature coupling, with cotton, corn, and tomato showing distinct responses across the Central Valley**. Same as Fig. S8 but for Cotton (a), Corn (e), and Tomatoes (i). (b), (f), and (j) same as Fig. 3b but for Cotton, Corn, and Tomatoes, respectively. (d), (h), and (l) represent the correlation between T and ET for (c) Cotton, (g) Corn, and (k) Tomatoes in lines for individual counties for Corn, Cotton, and Tomatoes, respectively.

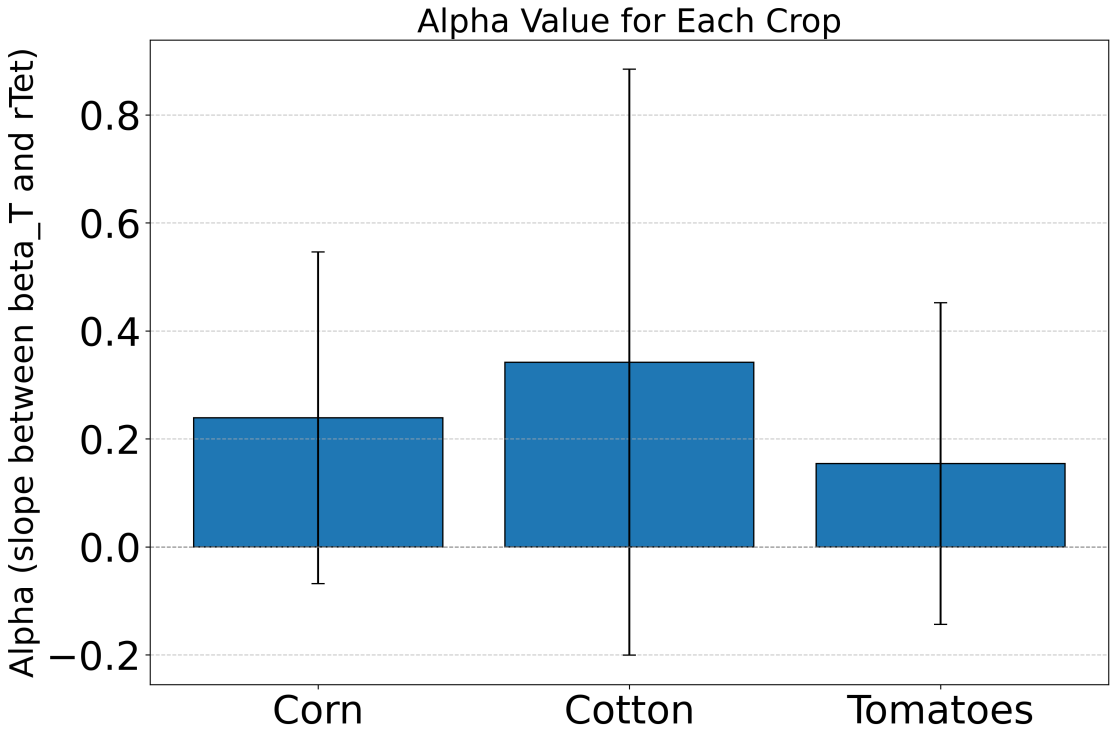

171

172 Fig. S25: **The sensitivity of crop yield response differs markedly among corn, cotton, and**
173 **tomatoes.** Linear regression between crop yield response $\hat{\beta}_T^{c,k}$ and correlation between T (°C) and
174 ET ($\hat{r}_{T,ET}{}^{c,k}$) (see Methods).

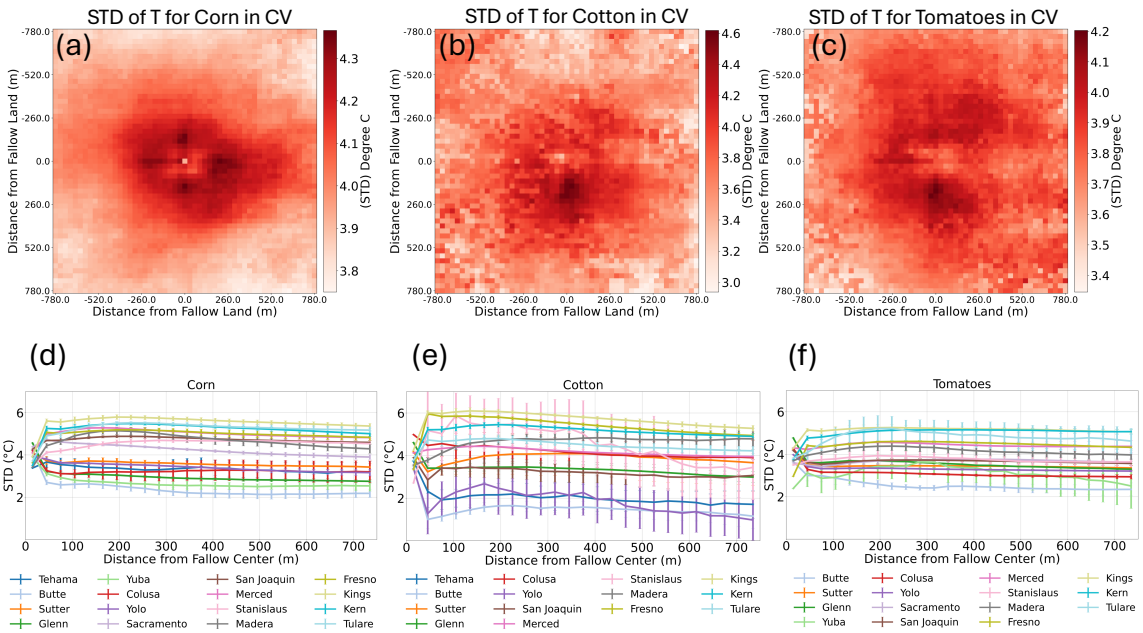

175

Fig. S26: **Temperature variability (STD of T, °C) differs among corn, cotton, and tomatoes and across counties.** Same as Fig. S5 but for STD (°C) of different crops, (a) Corn, (b) Cotton, and (c) Tomatoes, respectively. Lines in (d), (e), and (f) show STD (°C) for Corn, Cotton, and Tomatoes for individual counties.

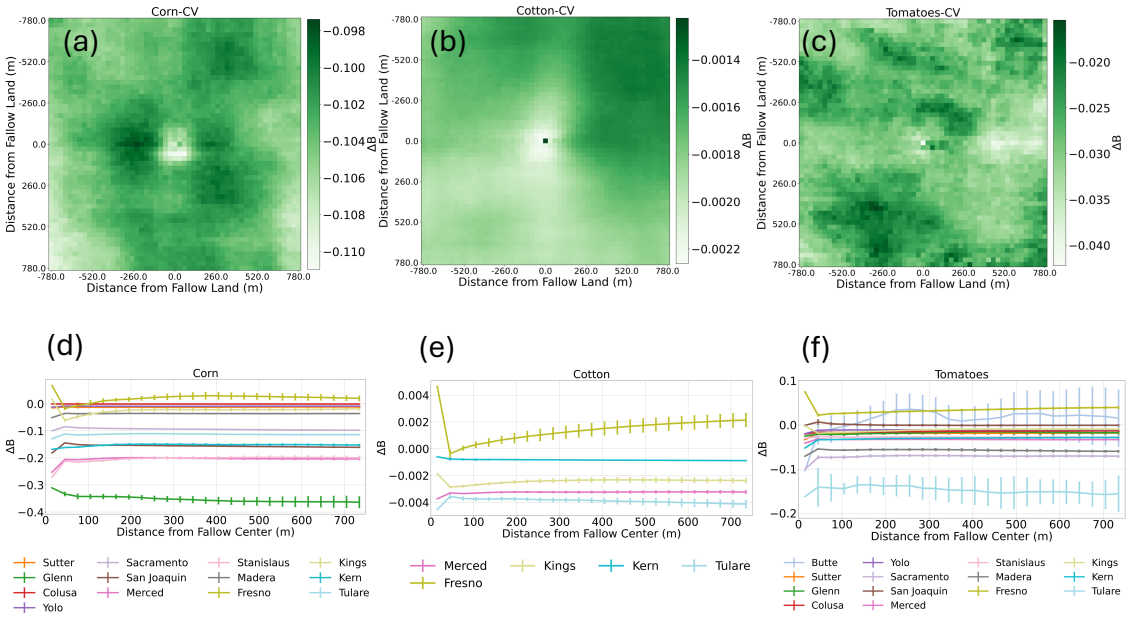

Fig. S27: **ΔB differs among corn, cotton, and tomatoes and across counties.** Same as Fig. S5 but for ΔB of different crops (a) Corn, (b) Cotton, and (c) Tomatoes, respectively. Lines in (d), (e), and (f) show ΔB for Corn, Cotton, and Tomatoes for individual counties.

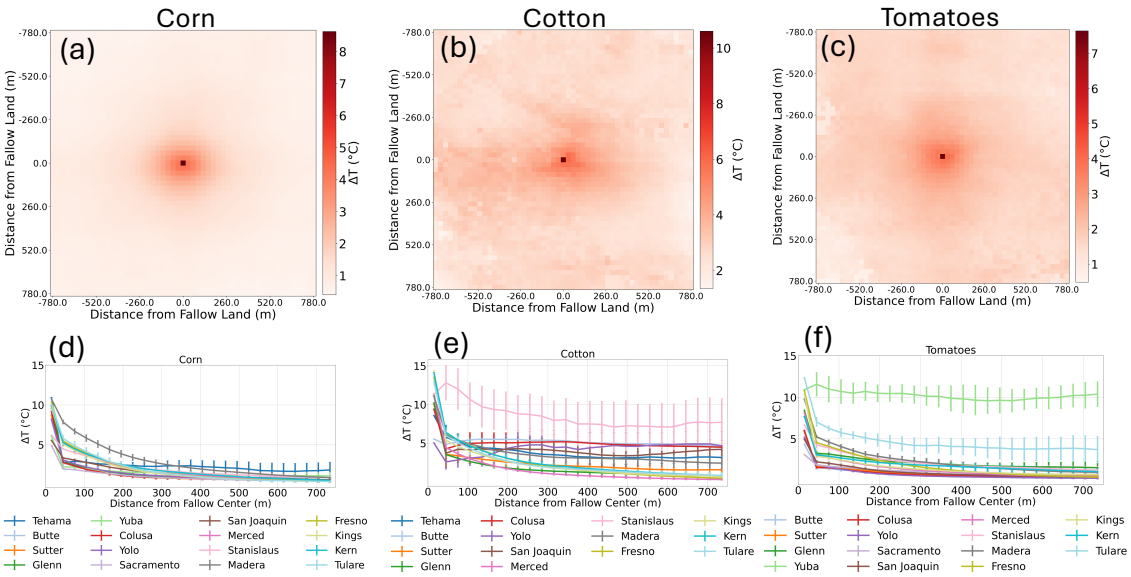

Fig. S28: **Temperature change ΔT (°C) differs among corn, cotton, and tomatoes and across counties.** Same as Fig. S5 but for ΔT of different crops (a) Corn, (b) Cotton, and (c) Tomatoes, respectively. Lines in (d), (e), and (f) show ΔT for Corn, Cotton, and Tomatoes for individual counties.

208 **Table 1**: Crop types included within each crop category analyzed in this study, corresponding to
209 the classifications used in Fig. S6 and Fig. S9.

Crop Categories	**Crop Type**
Citrus Subtropical	Citrus, Olives, Oranges, Avocados
Corn and Cotton	Corn, Cotton, Sweet Corn, Pop or Orn Corn
Deciduous Fruits and Nuts	Cherries, Peaches, apples, Other Tree Crops, Pecans, Almonds, Walnuts, Pears, Pistachios, Prunes, Pomegranates, Nectarines, Plums, Apricots
Double Field and Grain	Dbl Crop WinWht/Soybeans, Dbl Crop WinWht/Corn, Dbl Crop Oats/Corn, Dbl Crop Triticale/Corn, Dbl Crop Lettuce/Durum Wht, Dbl Crop Lettuce/Cantaloupe, Dbl Crop Lettuce/Barley, Dbl Crop Durum Wht/Sorghum, Dbl Crop Barley/Sorghum, Dbl Crop WinWht/Sorghum, Dbl Crop Barley/Corn, Dbl Crop WinWht/Cotton, Dbl Crop Soybeans/Cotton, Dbl Crop Soybeans/Oats, Dbl Crop Corn/Soybeans, Dbl Crop Barley/Soybeans
Field Crops	Sorghum, Soybeans, Sunflower, Peanuts, Tobacco, Millet, Speltz, Canola, Flaxseed, Safflower, Rape Seed, Mustard, Camelina, Sugar beets, Sugarcane, Hops
Truck Crops and Berries	Mint, Dry Beans, Potatoes, Other Crops, Sweet Potatoes, Misc Vegs & Fruits, Watermelons, Onions, Cucumbers, Chickpeas, Lentils, Peas, Tomatoes, Caneberries, Herbs, Carrots, Asparagus, Garlic, cantaloupes, Honeydew Melons, Broccoli, Peppers, Greens, Strawberries, Squash, Lettuce, Pumpkins, Blueberries, Cabbage, Cauliflower, Celery, Radishes, Turnips, Eggplants, Gourds, Cranberries

210

211 **Table 2:** Non-crops that were excluded from the CDL data in the analysis.

Fallowed Land	Barren
Wildflowers	Deciduous Forest
Grass Seeds	Evergreen Forest
Aquaculture	Mixed Forest
Open Water/Wetlands	Shrubland
Perennial Ice/Snow	Grassland
Developed/Open Space	Pasture
Developed/Low Intensity	Woody Wetlands
Developed/Mid Intensity	Herbaceous Wetlands
Developed/High Intensity	

212

213

214

215

Table 3: Years for which county-level crop yield data were available for each crop and county included in this study. The table lists the specific years where yield records were reported in the dataset, allowing identification of temporal coverage and data availability across different crops and counties.

Crops	Counties	Years of data
CORN	Colusa	2013, 2021
	Glenn	2014, 2015, 2016, 2018, 2019, 2021, 2022
	Yolo	2013, 2015, 2016, 2018, 2019
	Sutter	2013, 2014, 2016, 2018, 2019, 2021, 2022
	Sacramento	2013, 2014, 2015, 2016, 2018, 2019, 2021, 2022
	San Joaquin	2013, 2014, 2015, 2016, 2017, 2018, 2019, 2020, 2021, 2022
	Stanislaus	2013, 2014, 2015, 2016, 2017, 2018, 2019, 2020, 2021, 2022
	Merced	2013, 2014, 2015, 2016, 2017, 2018, 2019, 2020, 2021, 2022
	Madera	2013, 2014, 2016, 2017, 2020, 2021, 2022
	Fresno	2013, 2014, 2016, 2018, 2019, 2020, 2021, 2022
	Tulare	2013, 2014, 2015, 2016, 2017, 2018, 2019, 2020, 2021, 2022
	Kings	2013, 2014, 2015, 2016, 2018, 2019, 2020, 2021, 2022
	Kern	2013, 2014, 2015, 2016, 2017, 2020, 2021, 2022
Crops	**Counties**	**Years of data**

COTTON	Merced	2013, 2014, 2015, 2016, 2017, 2018, 2019, 2020, 2021, 2022
	Fresno	2013, 2014, 2015, 2016, 2017, 2020, 2021, 2022
	Kern	2013, 2016, 2020, 2022
	Kings	2013, 2014, 2015, 2016, 2017, 2018, 2019, 2020, 2021, 2022
	Madera	2013
	Tulare	2013, 2014, 2015, 2016, 2017, 2018, 2019, 2020, 2021, 2022
Crops	**Counties**	**Years of data**
TOMATOES	Tehama	2022
	Butte	2018, 2019, 2020, 2021, 2022
	Colusa	2013, 2014, 2016, 2017, 2018, 2019, 2020, 2021, 2022
	Glenn	2018, 2019, 2020, 2021, 2022
	Yolo	2013, 2014, 2015, 2016, 2017, 2018, 2019, 2020, 2021, 2022
	Sutter	2013, 2014, 2015, 2016, 2017, 2018, 2019, 2020, 2021, 2022
	Sacramento	2013, 2015, 2016, 2017, 2018, 2019, 2020, 2021, 2022
	San Joaquin	2013, 2014, 2015, 2016, 2017, 2018, 2019, 2020, 2021, 2022
	Stanislaus	2013, 2014, 2015, 2016, 2017, 2018, 2019, 2020, 2021, 2022
	Merced	2013, 2014, 2015, 2016, 2017, 2018, 2019, 2020, 2021, 2022

	Madera	2013, 2014, 2017, 2020, 2021, 2022
	Fresno	2013, 2014, 2015, 2016, 2017, 2018, 2019, 2020, 2021, 2022
	Tulare	2020, 2021
	Kings	2013, 2014, 2015, 2016, 2017, 2018, 2019, 2020, 2021, 2022
	Kern	2013, 2014, 2015, 2016, 2017, 2018, 2019, 2020, 2021, 2022

221